Atmos. Chem. Phys. Discuss., 15, 7783–7836, 2015
www.atmos-chem-phys-discuss.net/15/7783/2015/
doi:10.5194/acpd-15-7783-2015

Atmospheric Chemistry and Physics Discussions

Prognostic precipitation with three liquid water classes in the ECHAM5-HAM GCM

V. Sant[1,*], **R. Posselt**[2], **and U. Lohmann**[1]

[1]Institute of Atmospheric and Climate Science, ETH Zürich, Zürich, Switzerland
[2]Federal Institute for Meteorology and Climatology, MeteoSchweiz, Zürich, Switzerland
[*]now at: Max Planck Institute for Meteorology, Hamburg, Germany

Received: 9 February 2015 – Accepted: 27 February 2015 – Published: 12 March 2015

Correspondence to: V. Sant (vivek.sant@mpimet.mpg.de)

Published by Copernicus Publications on behalf of the European Geosciences Union.

Abstract

In order to improve the global representation of rain formation in marine stratiform clouds a new parameterization with three prognostic liquid water classes was implemented into the general circulation model ECHAM5 with the aerosol module HAM. The additionally introduced drizzle class improves the physical representation of the droplet spectrum and more importantly, improves the microphysical processes relevant for precipitation formation compared to the standard parameterization. In order to avoid a mismatch of the liquid and ice phase, the prognostic treatment of snow has been introduced too. This has a significant effect on the amount and altitude of ice clouds, which in turn does not only affect in- and outgoing radiation, but also the parameterized collection rates. With the introduction of a prognostic precipitation scheme a more realistic representation of both liquid and ice phase large-scale precipitation is achieved compared to a diagnostic treatment. An encouraging finding is that the sensitivity of the liquid water path to the anthropogenic aerosol forcing with the prognostic treatment is reduced by about 25 %. Although the total net radiative forcing is increased from 1.4 ± 0.4 to $1.6 \pm 0.4\,\mathrm{W\,m^{-2}}$ from the control to the prognostic model version, the difference is within the interannual variability. Altogether the results suggest that the treatment of precipitation in global circulation models has a significant influence on the phase and lifetime of clouds, but also hints towards the uncertainties related to a prognostic precipitation scheme.

1 Introduction

The challenge of projecting future climate, its sensitivity to anthropogenic forcing, the change in global precipitation patterns and the mitigation of climate change remains difficult and is closely linked to correctly representing the radiative forcing. The greatest uncertainty lies in the representation of clouds (e.g. Stephens, 2005), whether it is their fundamental coupling to the large-scale circulation (Stevens and Bony, 2013)

ACPD
15, 7783–7836, 2015

or their interaction with anthropogenic aerosols on the very fine scales (Boucher et al., 2013). As resolution in general circulation models (GCMs) remains coarse (O(100 km)), the improvements made on subgrid scale processes are a priori limited, may this be for the parameterization of convection, turbulence or microphysics, as all parameterizations are governed by the resolved larger scales. Nevertheless, understanding the dependence of the subgrid scale parameterizations and improving crude representations of subgrid scale processes is crucial for climate models to hopefully reduce the error in climate projections.

One of the largest uncertainties is the response of clouds and precipitation to changes in aerosol concentrations (Stevens and Feingold, 2009). Aerosols are necessary for the formation of clouds by acting as cloud condensation nuclei (CCN) or ice nuclei (IN) and changes in the CCN and IN number concentrations affect the number of cloud droplets or ice crystals. Thin, low level marine stratus and stratocumulus are known to be very susceptible to changes in aerosol concentration. Being very widespread, they constitute a major source of uncertainty in climate models (e.g. Bony and Dufresne, 2005). Traditionally an increase in aerosols is thought to ultimately lead to brighter clouds (Twomey, 1974) and maybe longer-lived clouds (Albrecht, 1989), reasoning that the increase in CCN leads to an increase in cloud droplets and consequently reduces the efficiency to form rain. Since cloud droplets have to first collide and coalesce to form small rain or drizzle drops (autoconversion), before upon further collection of cloud droplets by drizzle drops (accretion) a significant amount of rain is produced, an increase in cloud droplets can influence the precipitation formation. Where there is ample evidence for higher CCN concentrations leading to more cloud droplets, the subsequent effect on the cloud amount and precipitation is highly debated as the suppression of precipitation is found to be in competition with the evaporation by entrainment of dry air (Ackerman et al., 2004; Jiang et al., 2006), such that the suppression may not sustain (Boucher et al., 2013). Many GCMs do not have the ability to include such compensating effects on small scales, thus it is not surprising that for mixed or ice phase clouds, the influence of aerosols on the radiative budget

ACPD
15, 7783–7836, 2015

is still unclear (Boucher et al., 2013). For mixed phase clouds an increase in aerosols can lead to two competing effects namely the glaciation effect and the de-activation effect (Lohmann and Hoose, 2009). With more IN the cloud would glaciate and form precipitation more readily reducing its radiative effect. On the other hand, IN may also be coated with soluble material, i.e. sulfate, reducing its nucleation ability and having the contrary effect. Whether it is for liquid, mixed or ice phase clouds, describing the influence of aerosols on clouds and precipitation formation requires a whole chain of processes that need to be considered. Here the focus will be on the collection processes and the sensitivity of the model to the anthropogenic aerosol forcing.

The increase in aerosol concentrations since the preindustrial era, led to a negative radiative forcing corresponding to a cooling that partly offset the greenhouse gas warming (Boucher et al., 2013). The radiative forcing is comprised of (i) a direct influence of the aerosols on the in- and outgoing radiation and (ii) an indirect influence of aerosols by changing cloud properties. GCMs have shown to overestimate the cooling related to this aerosol-cloud-precipitation interactions compared to observations (Quaas et al., 2009). Posselt and Lohmann (2008a) showed that the diagnostic treatment of rain in GCMs results in an overemphasis of the autoconversion process, which leads to a high sensitivity of clouds and thus formation of precipitation to changes in aerosol concentrations. By introducing a prognostic treatment of rain, a more realistic partitioning between the autoconversion and accretion process can be achieved (Posselt and Lohmann, 2008a; Gettelman and Morrison, 2015). Further studies following suit (Reitter et al., 2011; Walters et al., 2014; Gettelman et al., 2015) or using a multi-scale modelling framework (Wang et al., 2011) confirm these findings, not only reducing the sensitivity of clouds and precipitation to the anthropogenic aerosol forcing, but also improving the representation of cloud ice and snow (Reitter et al., 2011) and reducing the frequency of unrealistic light rain (Walters et al., 2014).

As a follow-on to the work by Posselt and Lohmann (2008a) and Posselt and Lohmann (2009), where the importance of the drop size distribution (DSD) was recognized, this study focuses on the representation of both liquid and solid phase precip-

ACPD
15, 7783–7836, 2015

itation in the ECHAM5-HAM GCM and its response to the anthropogenic aerosol forcing. For the liquid phase, an intermediate drizzle drop class is introduced for a more physical representation of (i) the drizzling conditions often found in marine stratocumulus (van Zanten et al., 2005) and the effect it can have on the cloud top effective radius (Wood, 2000), and (ii) the shape of the DSD. By introducing the scheme by Sant et al. (2013) into the ECHAM5-HAM, which is based on truncated moments and is believed to be a more realistic representation of the DSD, the collection processes, i.e. autoconversion, accretion and self-collection, are adapted for the three liquid water classes of cloud, drizzle and rain. A weakness of the previous studies was the biased improvement of only the liquid phase, i.e. the treatment of snow remained diagnostic. Consequently, similar to the work done by Gettelman and Morrison (2015) and Gettelman et al. (2015) in the CAM5 model a full prognostic treatment of precipitation is introduced for drizzle, rain and snow.

The outline of the article is as follows. Section 2 will give a general description of the ECHAM5-HAM GCM and the changes made by introducing the prognostic treatment of precipitation. Results are presented in Sect. 3 starting with global fields before looking at the cloud properties and the precipitation microphysics. The section ends with the comparison of present day and preindustrial simulations. Finally, the conclusions are presented in Sect. 4.

2 Model description

2.1 ECHAM5-HAM GCM

For this study, the ECHAM5-HAM general circulation model (GCM) (Roeckner et al., 2003) coupled to the two-moment modal aerosol scheme HAM (Stier et al., 2005) as in Lohmann and Hoose (2009) is used. The model solves the prognostic equations for temperature, surface pressure, divergence and vorticity on a spectral grid with a triangular truncation. Within HAM the aerosol size distribution is represented by a superpo-

ACPD
15, 7783–7836, 2015

sition of 7 lognormal distributions describing the different sizes and solubilities for the compounds sulfate, black carbon, organic carbon, sea salt and mineral dust.

This ECHAM5 control version (CTRL) includes a two-moment stratiform cloud microphysics scheme for cloud droplets and ice crystals (Lohmann et al., 2007) coupled to the aerosol scheme HAM, and uses an empirical cloud cover scheme (Sundqvist et al., 1989). The microphysics scheme includes all phase changes between the water components (vapour, liquid and ice), the collection processes (autoconversion, accretion and aggregation), evaporation of rain, melting of snow and sedimentation of cloud ice (Lohmann et al., 2007). The activation of cloud drops follows the empirical activation scheme by Lin and Leaitch (1997), which depends on the aerosol number concentration and the sub grid-scale updraft velocity. Cirrus clouds form by homogeneous freezing of supercooled solution drops (Lohmann et al., 2008), which has been found to be the dominant freezing mechanism for these type of clouds (Kärcher and Ström, 2003). Although recently, this view has been questioned (Cziczo et al., 2013).

The CTRL version of the model treats precipitation diagnostically, i.e. it reaches the surface within one model time step or evaporates/sublimates in the sub-saturated air below the cloud. Following Khairoutdinov and Kogan (2000) for the collection processes, cloud and rain water are separated at a radius of 25 µm. However, the diagnostic treatment of rain is only realistic for drops larger than 100 µm, which lead Posselt and Lohmann (2008a) to the introduction of a prognostic rain scheme to account for the drizzling conditions often found in marine stratocumulus. Yet, one is still left with the rain class spanning all drops larger than 25 µm in radius, which tends to overestimate the number concentration of large drops and thus influences both the collection processes and the sedimentation. Consequently, we introduce drizzle ($25 < r < 100$ µm) as a third liquid water class and introduce the triclass parameterization by Sant et al. (2013) to describe the collection processes based on truncated moments. As mentioned before, prognostic equations for both liquid and ice phase precipitation are introduced for both mass and number for consistency, extending the CTRL version and referred to as PROG.

ACPD
15, 7783–7836, 2015

Note that with the introduction of the new collection scheme, due to the three liquid water classes, and the prognostic precipitation scheme, the parameter space for the tuning of the climate model (Lohmann and Ferrachat, 2010), i.e. to achieve radiative equilibrium, is changed. If the climate impacts of the schemes for both liquid and ice phase microphysics between the two model version CTRL and PROG are comparable, in terms of heating rates (Mauritsen et al., 2012), a similar climate can be expected. No other tuning parameters outside the cloud microphysics routine were changed as not to lose the comparability to the changes induced by the introduction of prognostic precipitation.

2.2 Prognostic precipitation

For the prognostic precipitation scheme the microphysical processes had to be restructured as illustrated by the flowchart in Fig. 1. In CTRL the microphysical processes are treated sequentially; first, the incoming precipitation fluxes (rain and snow) from the level above are modified by melting, sublimation and evaporation. This is followed by microphysical processes on cloud water and ice, i.e. condensation or evaporation, deposition or sublimation and freezing of cloud water. These processes do not interact with the precipitating water and for simplicity, will be referred to as the "phase changes". Then the conversion of cloud water (ice) to rain (snow) via autoconversion (aggregation) and the interaction of the two via accretion is calculated. The fluxes and tendencies of the given grid box are finally updated and the whole procedure is repeated for the next level down until reaching the surface.

For PROG the vertical loop is split into three loops; the first one computes the "phase changes", the second the formation of precipitation and its interaction with the cloud water and ice, and the third the sedimentation. The latter two are then subject to a sub-stepping over smaller time steps, i.e. time-splitting. Primarily, this is done to assure numerical stability of the sedimentation, as the Courant-Friedrichs-Levy (CFL) criterion needs to be met, and to improve the representation of the microphysical processes. Since the whole model could not be made subject to smaller time steps, the time-

ACPD
15, 7783–7836, 2015

splitting is only applied to processes relevant to the formation and sedimentation of precipitation. Furthermore, the splitting of the vertical loop is necessary as some cloud processes use a moisture adjustment scheme, which is not time dependent and would lead to inconsistencies if included in the time-splitting. The number of iterations needed for the time-splitting, i.e. the length of the sub-time step, depends on the fall speeds and the new triclass parameterization.

The rates for drizzle (d), rain (r) and snow (s) mass mixing ratio, $\partial q_i/\partial t$, $i \in \{\mathrm{d, r, s}\}$, and number concentration, $\partial N_i/\partial t$, can be summarized as follows

$$\frac{\partial q_\mathrm{d}}{\partial t} = b_\mathrm{c}(Q_{\mathrm{aut_c}} - Q_{\mathrm{aut_d}} + Q_{\mathrm{ac_{cd+}}} - Q_{\mathrm{ac_{cd-}}} - Q_{\mathrm{ac_{dr}}}) - (1 - b_\mathrm{c})Q_{\mathrm{evp_d}} + b_\mathrm{r}Q_{\mathrm{sed_d}} \quad (1)$$

$$\frac{\partial N_\mathrm{d}}{\partial t} = b_\mathrm{c}(P_{\mathrm{aut_c}} - P_{\mathrm{aut_d}} - P_{\mathrm{ac_{cd\text{-}}}} - P_{\mathrm{sc_d}}) - (1 - b_\mathrm{c})P_{\mathrm{evp_d}} + b_\mathrm{r}P_{\mathrm{sed_d}} \quad (2)$$

$$\frac{\partial q_\mathrm{r}}{\partial t} = b_\mathrm{c}(Q_{\mathrm{aut_d}} + Q_{\mathrm{ac_{cr}}} + Q_{\mathrm{ac_{cd\text{-}}}} + Q_{\mathrm{ac_{dr}}}) - (1 - b_\mathrm{c})Q_{\mathrm{evp_r}} + b_\mathrm{r}(Q_{\mathrm{mlt}} + Q_{\mathrm{sed_r}}) \quad (3)$$

$$\frac{\partial N_\mathrm{r}}{\partial t} = b_\mathrm{c}(P_{\mathrm{aut_d}} + P_{\mathrm{ac_{cd\text{-}}}} - P_{\mathrm{sc_r}}) - (1 - b_\mathrm{c})P_{\mathrm{evp_r}} + b_\mathrm{r}(P_{\mathrm{mlt}} + P_{\mathrm{sed_r}}) \quad (4)$$

$$\frac{\partial q_\mathrm{s}}{\partial t} = b_\mathrm{c}(Q_{\mathrm{agg}} + Q_{\mathrm{ac_s}}) - (1 - b_\mathrm{c})Q_{\mathrm{sub}} + b_\mathrm{r}(-Q_{\mathrm{mlt}} + Q_{\mathrm{sed_s}}) \quad (5)$$

$$\frac{\partial N_\mathrm{s}}{\partial t} = b_\mathrm{c}P_{\mathrm{agg}} + b_\mathrm{r}(-P_{\mathrm{mlt}} - P_{\mathrm{sec}} + P_{\mathrm{sed_s}}), \quad (6)$$

where $Q_{(.)}$ and $P_{(.)}$ account for changes in mass and number, respectively, and the cloud and precipitation fraction are denoted by b_c and b_r, respectively. The source and sink terms related to the triclass parameterization for the collection processes are given in Sant et al. (2013) with some adjustments discussed later. For clarity all acronyms are summarized in Table 1.

For the ice microphysical processes the same parameterizations used in CTRL are also used in PROG. However, where the number concentrations of the precipitating hydrometeors did not need to be determined in CTRL, they are indispensable in PROG,

ACPD
15, 7783–7836, 2015

whereby certain assumptions are necessary. During the evaporation of drizzle and rain drops a constant mean mass is assumed, hence the change in mass is followed by an associated equal fractional change in number density. As pointed out by Seifert (2008), this assumption holds rather well for drizzling stratocumulus (e.g. Khairoutdinov and Kogan, 2000). Following the formulation by Levkov et al. (1992) for the production of snow as described in Lohmann and Roeckner (1996), the created snow mass by aggregation was assumed to have a minimum diameter of 200 µm. This assumption together with the mass-length relation by Spichtinger and Gierens (2009) was used to determine the snow flake number concentration. When snow crystals melt they are assumed to be a source term for the rain drops, where one snow crystal is assumed to produce one rain drop. Note that the gain of snow mass due to accretion is assumed not to change the number of snow crystals.

2.2.1 Sedimentation

Following Posselt and Lohmann (2008a, 2009) and Müller (2007), the sedimentation of all three precipitating hydrometeor types, i ($\in \{\mathrm{d}, \mathrm{r}, \mathrm{s}\}$), is treated as a vertical 1-D-advection with the mass and number weighted fall velocities v_{q_i} and v_{N_i} for the mass and number density, q_i and N_i, respectively, allowing for gravitational sorting. Numerically an explicit Euler scheme was used, which by definition conserves mass. As described in Posselt and Lohmann (2008a) the sedimentation velocities are derived by using the flux density approach by Srivastava (1978, Eqs. 48 and 49) for both mass and number, respectively,

$$\mathfrak{F}_{q_i} = q_i v_{q_i} = \frac{\pi}{6}\rho_\mathrm{w} \int_0^\infty D^3 f_i(D) v_{\mathrm{t},i}(D)\,\mathrm{d}D \tag{7}$$

$$\mathfrak{F}_{N_i} = N_i v_{N_i} = \int_0^\infty f_i(D) v_{\mathrm{t},i}(D)\,\mathrm{d}D, \tag{8}$$

ACPD
15, 7783–7836, 2015

where ρ_w is the density of water and $v_{t,i}$ is the terminal velocity of the corresponding hydrometeor with diameter D. Note that with this approach, changes in mass density with height, due to changes in air density, are taken into account. Following Posselt and Lohmann (2009) the number density function f_i is assumed to follow a gamma distribution of the form

$$f_i(D) = \frac{N_i}{\Gamma(\mu_i) D} \left(\frac{D}{D_{0,i}}\right)^{\mu_i} \exp\left(-\frac{D}{D_{0,i}}\right), \tag{9}$$

where $\Gamma(.)$ is the Gamma function, μ_i is a free shape parameter and $D_{0,i}$ is related to the mean diameter $\overline{D}_i$ by

$$D_{0,i} = \frac{\overline{D}_i}{\sqrt[3]{\mu_i(\mu_i+1)(\mu_i+2)}} \tag{10}$$

with

$$\overline{D}_i = \sqrt[3]{\frac{6}{\pi \rho_w} \frac{\rho_a \, q_i}{N_i}}. \tag{11}$$

By determining the terminal velocity $v_{t,i}(D)$ of a single drop or crystal, Eqs. (7) and (8) can be solved for the bulk fall velocities v_{q_i} and v_{N_i}.

For the liquid phase, i.e. drizzle and rain drops, the terminal velocity of a single drop was determined using an approximated expression based on Rogers et al. (1993). Integrating equations (7) and (8) yields the bulk fall velocities (cf. Posselt and Lohmann, 2009)

$$v_{q_i} = \begin{cases} (\mu_i + 3) b_v D_{0,i}, & \text{for } D_{0,i} \le D_v/(\mu_i+3) \\ b_1, & \text{for } D_{0,i} > D_v/(\mu_i+3) \end{cases} \tag{12}$$

$$v_{N_i} = \begin{cases} \mu_i b_v D_{0,i}, & \text{for } D_{0,i} \le D_v/\mu_i \\ b_1, & \text{for } D_{0,i} > D_v/\mu_i \end{cases}, \tag{13}$$

ACPD
15, 7783–7836, 2015

where the constant $b_v = b_3(b_2 - 5(b_2 - b_1)) = 3918\,\mathrm{s}^{-1}$ and the critical distribution parameter D_v is given by $D_v = b_1/b_v = 2463\,\mu\mathrm{m}$. Equations (12) and (13) are used for both drizzle and rain drops, where the shape parameters μ_d and μ_r were chosen assuming a constant value of $\mu_\mathrm{d} = \mu_\mathrm{r} = 5$. This choice follows the findings by Posselt and Lohmann (2009) and results in a distribution width, which is not too wide as to not overestimate the number of large drops, but wide enough to enable gravitational sorting. A direct link to the assumed distributions for the collection processes cannot be made, as sedimentation is based on grid mean values whereas the collection rates are based on in-cloud values. This incoherence should be avoided in future climate models. Note that for large $D_{0,i}$ or μ_i gravitational sorting does not occur anymore as v_{q_i} and v_{N_i} converge. In this case $\overline{D}_i$ would have to be approximately 2 mm or larger, a regime not found in our simulations.

For snow flakes the terminal fall velocity of a single snow crystal is determined following Barthazy and Schefold (2006)

$$v_{\mathrm{t},i}(D) = \beta_1 D^{\beta_2} \tag{14}$$

assuming irregular crystals with $\beta_1 = 1.23$ and $\beta_2 = 0.22$, where the diameter was again determined using the mass-length relation by Spichtinger and Gierens (2009). Repeating the procedure as for the liquid phase assuming the same number distribution $f_i(D)$ yields the following bulk fall velocities for snow

$$v_{q_\mathrm{s}} = \beta_1 D_{0,i}^{3+\beta_2} \frac{\Gamma(3 + \mu_\mathrm{s} + \beta_2)}{\Gamma(3 + \mu_\mathrm{s})} \tag{15}$$

$$v_{N_\mathrm{s}} = \beta_1 D_{0,i}^{\beta_2} \frac{\Gamma(\mu_\mathrm{s} + \beta_2)}{\Gamma(\mu_\mathrm{s})}. \tag{16}$$

For consistency with Levkov et al. (1992), it is assumed that the size distribution of snow follows an exponential distribution, i.e. $\mu_\mathrm{s} = 1$.

ACPD
15, 7783–7836, 2015

2.2.2 Collection processes

In CTRL the collection processes responsible for the formation of precipitation follow the formulation by Khairoutdinov and Kogan (2000). With the introduction of drizzle as a third liquid water class in PROG, the collection processes of autoconversion, accretion and self-collection are reformulated using the scheme by Sant et al. (2013). By solving the stochastic collection equation for truncated moments, two-moment rate equations are derived for cloud, drizzle and rain mass and number densities. However, as the scheme is computationally rather expensive, especially for the numerical solution of contained integrals, an approximation is presented here. The integrals in question (cf. Sant et al., 2013, Appendix B) are normalized by the number concentration and then approximated by a polynomial in log-space with a non-linear least square fit using a Levenberg–Marquardt algorithm (Press et al., 1992). The details of the approximation are presented in the Appendix.

This approximation introduces a small error, mainly due to the integral used for the accretion between cloud and drizzle drops, as the dependence on the shape parameters and the continuity condition are larger than for the other approximated integrals (cf. Sant et al., 2013). Tests have shown that the error is within a few percent of the produced precipitation. This is very reasonable, especially in view of reduced computational cost. The approximation reduces the model calculation by about a factor of 2.5, leaving the calculation of PROG to be a factor of 2.5 – instead of 6 – higher than CTRL. These numbers are based on a time step of 30 s for the time-splitting.

3 Results

3.1 Model setup

All global simulations presented here are conducted at a horizontal resolution of T63 ($\sim 1.875^\circ \times 1.875^\circ$) with 31 vertical levels, where the uppermost level interface is at

ACPD
15, 7783–7836, 2015

10 hPa. For PROG the model time step of 12 min is divided into 24 sub-time steps for all precipitation processes as described above, such that a time step of 30 s is reached for the time-splitting. Using climatological sea surface temperatures and sea-ice extent the simulations are integrated for 5 years (2000–2004) after a spin-up of 3 months. For a closer look at in-cloud processes further statistics were made based on 6 hourly data of the first month of the year 2000. This proved to be sufficient to get a good sampling of the parameter space.

To estimate the total anthropogenic aerosol effect, which is the change of the net radiation at the top of the atmosphere (TOA) due to anthropogenic aerosols, simulations with present-day (PD) and pre-industrial (PI) aerosol emissions integrated over the same 5 years are compared. The PI simulations use natural aerosol emissions representative of the year 1750 (Dentener et al., 2006).

3.2 Present day results

3.2.1 Global and zonal fields

The global and zonal annual mean cloud properties and TOA energy budget are presented in Table 2 and Fig. 2, respectively, for the simulations with PROG and CTRL, together with observations for comparison. The total precipitation amount is very similar in both PROG and CTRL, both overestimating the observed amount from the Global Precipitation Climatology Project (GPCP) dataset of the years 1979–2001 (Adler et al., 2003). The overestimation is mainly located in the tropics and subtropics as can be seen in Fig. 2a. Separating the total precipitation into stratiform, i.e. large-scale, and convective precipitation a shift to more stratiform precipitation in PROG can be deduced, at the same time reducing the amount of convective precipitation. Although the differences in the zonal mean are not very pronounced (cf. Fig. 2b and d), the largest difference between PROG and CTRL is seen in stratiform precipitation in the tropics. In addition, the fraction of stratiform precipitation falling as snow is shown in Fig. 2c, where a slight shift towards the tropics is seen in PROG. In general, the prognostic

ACPD
15, 7783–7836, 2015

treatment of both warm and cold precipitation (drizzle, rain and snow) has little effect on the precipitation amount reaching the surface, which is to be expected as we are using climatological sea surface temperatures (SSTs). Since the SSTs determine the evaporation rates over the ocean and precipitation is balanced by the amount of evaporation, the differences in precipitation amount need to be small. Nevertheless, the hydrological cycle can be altered by increasing or decreasing the cloud lifetimes through the microphysical collection processes, which will be addressed later.

The simulated total cloud cover (TCC) is within the range of observations for both PROG and CTRL, differing by about one percent. The differences are located in the northern mid-latitudes as can be seen in Fig. 2e.

The prognostic treatment of precipitation has a large effect on both liquid and ice water paths globally and on the zonal mean (cf. Fig. 2f–h). In a global mean the liquid water path (LWP) is 7 % smaller in PROG (69.2 compared to 74.2 g m^2 in CTRL), where both are within the range of observations. Over the oceans, PROG exhibits a smaller LWP in the Southern Hemisphere, but a higher peak in the tropics compared to CTRL (cf. Fig. 2f and g). Over the Northern Hemisphere ocean the differences between the two simulations are negligible, however taking the land into account (cf. Fig. 2h) reveals that the reduction in LWP is located in the mid-latitudes of both hemispheres, where stratiform clouds are dominant. On the other hand, the ice water path (IWP) is about 60 % larger in PROG and although still strongly underestimating the observations, it can be seen as an improvement. Summed up (LWP + IWP, not shown) the LWP dominates the zonal mean, where PROG shows a reduced water path in the mid-latitudes but a larger peak in the tropics. In general, the peaks in both LWP and IWP in the tropics are in better agreement with observations. On a further note, the frequency of occurrence of both liquid and ice clouds have decreased from CTRL to PROG. For the liquid phase clouds the lifetime decreased by about 30 % (10 % of the time there is a cloud in the lowest 8 model levels in PROG compared to about 14 % of the time in CTRL), whereas for ice clouds the decrease was about 5 %, respectively (same values are valid for the occurrences of the corresponding PI simulations). This shows, in

ACPD
15, 7783–7836, 2015

particular for the liquid clouds, that the hydrological cycle is faster in PROG than in CTRL.

The prognostic scheme also has a significant impact on the vertically integrated cloud droplet number concentration (CDNC burden) and the ice crystal number concentration (ICNC burden), reducing them by 3 % and nearly 25 %, respectively, from CTRL to PROG. The effects are most prominent in the mid-latitudes and especially large for the ICNC burden (cf. Fig. 2i and j). The reason for these effects and the relation to the water paths will be discussed in more detail below.

The link between the cloud properties and the TOA radiative effects is a little more intricate. The reduced LWP and cloud lifetime in PROG compared to CTRL has increased the shortwave cloud radiative effect (SWCRE, notation used as in Boucher et al., 2013) by nearly $3\,W\,m^{-2}$ in the global mean, which means that less shortwave radiation is reflected back to space. In the zonal-mean shown in Fig. 2k, this increase can be found again in mid-latitudes corresponding to the location of the largest changes in LWP. The longwave cloud radiative effect (LWCRE) tends to be more sensitive to the TCC. As the reduction in TCC is not very large it cannot account for the reduction of $3\,W\,m^{-2}$ in PROG compared to CTRL. As the increase in IWP is accompanied by a decrease in ICNC burden in PROG, the ice crystals are larger, causing a reduction in the optical depth of ice clouds. The reduction of TCC and in ice clouds optical depth are the reason for the reduction in LWCRE (Fig. 2l).

As the changes in SWCRE and LWCRE compensate each other, the net total radiative effect at TOA (F_{net}) hardly changed from CTRL to PROG. Note that CTRL is tuned to be in equilibrium and it is rather remarkable that without any further tuning the new prognostic scheme results in a similar climate.

The aerosol optical depth (AOD) has been reduced in PROG by around 17 % with respect to CTRL and is certainly related to the prognostic treatment of precipitation. First, the precipitation takes longer to reach the surface and can therefore be a more effective sink through wet-deposition. Second, the increased hydrological cycle men-

ACPD
15, 7783–7836, 2015

tioned above ensures that the aerosol particles are washed out more frequently than in CTRL.

3.2.2 Cloud properties

The introduction of a prognostic precipitation scheme has a particularly strong influence on the IWP and the ICNC burden. The zonal mean ice water content (IWC) shown in Fig. 3 shows that the IWC has not only increased in PROG compared to CTRL, but that ice clouds are more frequent in lower altitudes, in particular close to the annual mean melting line. Compared to annual mean ERA-interim reanalysis (Dee et al., 2011) for the years 2000–2004, the known underestimation of IWC by the ECHAM5-HAM model is clearly visible. Thus, the higher IWC values in PROG and the shift to lower altitudes is in better agreement with the ERA-interim reanalysis. Consequently, the reduced LWCRE using prognostic precipitation is additionally due to the lower lying ice clouds. As the ICNC burden is reduced with higher IWC, the average ice crystal size is larger and therefore ice crystals sediment faster, resulting in clouds at lower altitudes. The reason for the reduced ICNC burden is caused by a change in collection rates and will be addressed later.

For the liquid water content (LWC) shown in Fig. 4 the prognostic treatment has lead to an overall reduction. Comparing zonal mean LWC in PROG and CTRL (cf. Fig. 4a and b), CTRL has a higher LWC, especially in midlatitudes. Note that the annual mean melting lines are only given as a guidance for the comparison to the IWC. With respect to the ERA-interim reanalysis clear differences are seen; in the midlatitudes both PROG and CTRL overestimate the LWC, whereas towards the tropics the low altitude clouds are missing and LWC at higher altitudes is overestimated. Although PROG shows a tendency to have a few more liquid water clouds in lower altitudes in the subtropics, there are too many liquid water clouds close to the surface, a bias already exhibited by CTRL that remains to be addressed.

The LWC difference between the two model versions (cf. Fig. 4c) shows that below the melting line LWC is enhanced in PROG, but reduced above it. The hypothesis is

ACPD
15, 7783–7836, 2015

that due to the higher IWC in general and particularly above the melting layer, supercooled liquid water is more rapidly depleted trough the Wegener-Bergeron-Findeisen process in PROG compared to CTRL. The difference in relative humidity depicted in Fig. 5a helps to underline this hypothesis as large regions above the melting layer are dryer by up to 6 %. On one hand, this correlates with the higher IWC values and on the other, it makes the formation of new liquid water clouds less probable, as a relative humidity based cloud cover scheme is used (Sundqvist et al., 1989). Vice versa, the enhanced LWC in the tropics can be explained by the enhanced relative humidity in the regions below the melting layer of up to 4 %, the reasons for which have not been clarified yet. Figure 5b also shows the difference in cloud cover between PROG and CTRL, which although small (below ±3 %), is dominated by the reduction of ice clouds in the midlatitudes and enhanced liquid clouds in the tropics.

3.2.3 Precipitation microphysics

With the introduction of prognostic precipitation (PROG) the global mean precipitation rate did not change much compared to the reference simulation (CTRL). However, as precipitation is balanced by the amount of evaporation and we are using climatological sea surface temperatures, which determine the evaporation rates over the ocean, this is not surprising. Nevertheless, the microphysical processes related to precipitation may well be altered; (i) by the introduction of a third liquid water class, i.e. drizzle, and the altered collection rates, and (ii) by the time splitting of the precipitation related microphysics.

Opposed to the diagnostic treatment in CTRL, PROG prognostically sediments and keeps precipitation in the atmosphere from one time step to the next. Figures 6a–c show the drizzle, rain and snow water contents (DWC, RWC and SWC), respectively, with the contour lines of the LWC and the IWC overlaid. The highest DWCs are found in the midlatitudes, which correlate well with the largest values in LWC, as expected. The values are larger at lower altitudes due to the effect of gravitational sorting. For the RWC the values are one order of magnitude larger, not only because of the larger drop

ACPD
15, 7783–7836, 2015

sizes, but in particular because of the additional source from the melting of snow. Especially in the tropics this is the case, where the RWC correlates better with the IWC and SWC than with the LWC. As expected, the SWC is well correlated with the IWC, since it is the only source for snow. The largest values are just above the melting line, again an effect of the gravitational sorting but also due to the continuous accretion of ice water, especially as the accretion rate is temperature dependent being higher at warmer temperatures. Below the melting line the SWC decreases rapidly, where it melts and forms rain. Compared to other studies (Reitter et al., 2011; Wang et al., 2011; Gettelman et al., 2015), the amount of snow in the atmosphere is an order of magnitude smaller. The reason for which could be the treatment of the collection processes, melting or sedimentation. Future work will address this issue.

To assess the effects of changes in the microphysics of both the liquid and ice phase, 6 hourly data of January 2000 for both PROG and CTRL were used for further analysis. As we are only interested in how the different processes change for a given state of the cloud, the amount of data is sufficient for good statistics.

In Fig. 7a–c the frequency of occurrence of instantaneous surface precipitation, liquid water path and ice water path are shown, respectively, for both CTRL and PROG. The instantaneous surface precipitation shows a clear shift to much larger values in PROG, having its peak around 65 mm day^{-1}, but all together has fewer precipitation events. In contrast, CTRL overall has more events, but the peak instantaneous surface precipitation is around 2 mm day^{-1}, which includes a lot of light rain events. As shown for the global MetUM model in Walters et al. (2014), the prognostic treatment of precipitation has largely reduced these light rain events and is producing more realistic surface precipitation amounts. The distribution of instantaneous LWP has not changed significantly, except that there has been a slight shift to larger values in PROG. However, for the distribution of instantaneous IWP both simulations differ quite significantly. CTRL exhibits a somewhat bimodal distribution, with a small peak around 10 g m^{-2} and a very distinct peak around 63 g m^{-2}. In PROG the IWP is clearly unimodal with

ACPD
15, 7783–7836, 2015

its maximum around 18 g m^{-2}, but also has a much larger tail towards larger values, all leading to the increased global annual mean values discussed before.

For the collection processes in the liquid phase the vertically integrated monthly mean cloud autoconversion (AU = aut$_c$) and accretion rates (AC = ac$_{cd}$ + ac$_{cr}$) are shown in Figs. 8 and 9 for CTRL and PROG, respectively. Figure 8 shows that in the CTRL simulation AU and AC are comparable such that the fraction of AU to the total conversion rate (AU + AC) is well above 30 % in most regions. It increases with increasing stratiform precipitation and therefore increases towards high latitudes (cf. Fig. 2). This overestimation of AU is well known in global models with diagnostic treatment of rain (e.g. Posselt and Lohmann, 2008a; Gettelman et al., 2013). By introducing the prognostic treatment of drizzle and rain in PROG the fraction of AU to the total conversion rate is strongly reduced to values well below 6 % as can be seen in Fig. 9. Although AU is of similar magnitude, AC has increased drastically. The global mean burdens are given in Table 3 and illustrate these conclusions again. Effectively, AC has increased by nearly two orders of magnitude from CTRL to PROG, the reasons for which is the longer lifetime of drizzle and rain in the cloud.

To understand the differences in AU from CTRL to PROG, instantaneous values of AU as a function of the mean effective cloud droplet radius for both CTRL and PROG are shown in Fig. 10. At large mean radii, the autoconversion rates of PROG are an order of magnitude higher than in CTRL. However, the scheme in PROG exhibits a threshold type behaviour, such that below an effective radius of 10 µm the amount of mass transferred to drizzle is negligible. While such a threshold does not exist in nature, model studies and observations suggest that cloud droplets need to grow beyond 12–14 µm for a significant amount of rain to be produced (Rosenfeld et al., 2012), i.e. for growth by collision-coalescence to dominate over diffusional growth. CTRL has a more gradual decrease and has autoconversion rates which are several orders of magnitude larger than PROG at effective radii below 10 µm. Although, one may argue that this is needed to produce a realistic amount of rain in a diagnostic scheme, it is not physical. Thus, the new prognostic scheme allows for a more physical representation not

ACPD
15, 7783–7836, 2015

only of the sedimentation of hydrometeors, but consequently also for the microphysical processes.

Similarly for the ice phase, the mean vertically integrated aggregation (AG = agg) and accretion (ACi = ac_s) rates are shown in Figs. 11 and 12 for CTRL and PROG, respectively. In contrast to the liquid phase, ACi is lower than AG in both simulations, such that AG makes up around 68 % and even 85 % of the total collection rate in the global mean for CTRL and PROG, respectively (cf. Table 3). The values for AG and ACi have both increased significantly in PROG, which is mainly due to the large increase in IWC, but also because of the occurrence of cloud ice at lower altitudes, since both AG and ACi increase at warmer temperatures. This increase stems from the increase in the quasi liquid layer with increased temperature, in turn causing the sticking efficiency to increase. Since the ratio of AG/ACi is not known on these scales and it constitutes a combination of complex processes, we cannot conclude if the prognostic treatment of snow has lead to a more realistic treatment of the ice phase processes. Nevertheless, these results suggest that within the framework of a prognostic precipitation scheme AG plays the dominant role in the total collection rate. However, note that as the actual collection processes for the ice phase have not been changed from CTRL to PROG, an overestimation of AG or ACi cannot be excluded due to the applied time splitting. The suitability of the collection processes needs to be further tested, e.g. whether the assumption of a smallest snow crystal size in the aggregation process needs to be adjusted under a prognostic scheme (Eidhammer et al., 2014).

3.3 Present day vs. preindustrial climate

To evaluate the total anthropogenic aerosol effect, pre-industrial (PI) simulations where performed for both CTRL and PROG. Global annual mean values are also summarized in Table 2 and the differences (PD – PI) in zonal annual mean averages of selected quantities are shown in Fig. 13.

The differences in global annual mean from PI to PD in precipitation amount and total cloud cover are small, i.e. on the order of a few percent, in both CTRL and PROG,

ACPD
15, 7783–7836, 2015

which is mainly due to the use of climatological sea surface temperatures as mentioned before. Consequently, the slight increase in precipitation and slight reduction in total cloud cover cannot be attributed to a specific process.

The LWP and CDNC burden have increased significantly in the Northern Hemisphere due to the increase in aerosol concentration from PI to PD for both CTRL and PROG. The PROG simulation reduces the increases in both LWP and CDNC in the Northern Hemisphere, but not as pronounced as the factor two found in a previous study (Posselt and Lohmann, 2009). The increase in CDNC and LWP leads to an increase in SWCRE as shown in Fig. 13a, c and e. In addition to the total water path, the SWCRE is also influenced by TCC (cf. Fig. 13b), which could explain the double peak in the Northern Hemisphere of the SWCRE change in PROG. Furthermore, note that the change in TCC at the equator has opposite signals in PROG and CTRL, leading to a negative SWCRE in PROG, but a positive SWCRE in CTRL.

The change in LWCRE (cf. Fig. 13f) is rather noisy and not significant in a global mean, but seems to correlate with the change in IWP which has not changed significantly (not shown). Interesting is that the rather large change in ICNC burden in CTRL (approximately 14 % with respect to PD in a global mean) has little effect on the radiation balance (cf. Fig. 13d and f). On the other hand, the changes in ICNC burden in PROG are negligible.

As the anthropogenic aerosol forcing mainly influences liquid water clouds, the change in shortwave radiation is dominant and leads to a net negative radiative forcing from PI to PD for both CTRL and PROG. Following Wang et al. (2011, cf. their Fig. 16) the sensitivity of the LWP to changes in CCN concentrations is shown in Fig. 14a and b for CTRL and PROG, respectively. The figures show boxplots and linear regression lines of the relative changes [(PD – PI)/PI] in annual mean LWP vs. the relative changes in annual mean activated CCN concentrations averaged over the lowest 8 model levels (surface to about 800 hPa). From the regression lines it can be deduced that with the prognostic treatment of precipitation a 30 % decrease in slope, and hence, lower sensitivity of the LWP to the aerosol forcing can be achieved. Furthermore, the

ACPD
15, 7783–7836, 2015

resulting slope in PROG is very similar to the one found by Wang et al. (2011) using the MMF model. The spread in change of LWP at low changes in CCN is slightly larger in PROG than for CTRL, but at larger values the spread in CTRL is significantly larger. In fact, for CTRL the larger the change in CCN the larger and broader the change in LWP becomes, whereas for PROG the spread tends to become narrower. In PROG the spread of the data tends to level off, but not necessarily the mean values (illustrated by the stars in Fig. 14a and b).

The total net radiative effect of the anthropogenic aerosol forcing (ERFaci + ari; Boucher et al., 2013) in terms of TOA energy balance (F_{net}) is a cooling of around $1.4 \pm 0.4\,W\,m^{-2}$ for CTRL and $1.6 \pm 0.4\,W\,m^{-2}$ for PROG, respectively, where the error estimation corresponds to the interannual SD. Both model versions overestimate the inverse estimate of $1.1 \pm 0.4\,W\,m^{-2}$ by Murphy et al. (2009) and fall towards the negative end of the ERFaci + ari estimate in Boucher et al. (2013). The difference of about $0.2\,W\,m^{-2}$ between CTRL and PROG can mainly be attributed to the differences in the Northern Hemisphere and in particular around the equator, where the two simulations have opposing F_{net}. The reason for the enhanced LWP and TCC in the tropics of PROG has not been clarified and will need further attention, but is likely related to the coupling of the large scale clouds to the convective cloud scheme. In addition, considering that the tuning parameters in PROG are the same as in CTRL, except for the autoconversion and accretion rates of cloud liquid water altered by the new collection scheme, this could be a measure of uncertainty in the current model setup. Further tests and sensitivity studies are necessary to deduce what is mainly due to compensating errors and where model errors dominate.

4 Conclusions

We have introduced a prognostic precipitation scheme for both the liquid and ice phase for which the precipitation microphysics, i.e. melting and evaporation of precipitation, collection rates, and sedimentation, are subject to a time splitting. For the liquid phase,

ACPD
15, 7783–7836, 2015

drizzle was introduced in addition to the existing cloud and rain water classes. Based on the triclass parameterization by Sant et al. (2013) the collection rates for autoconversion, accretion and self-collection were changed to account for the three classes. The ice phase microphysics scheme remained unchanged. Without any further tuning of the model the simulations compare well to observations and display clear improvements in modeled physics.

Improvements in the liquid phase are equivalent to other studies (Posselt and Lohmann, 2008a; Gettelman et al., 2015), where the prognostic treatment has lead to a better partitioning of the collection processes and consequently to an improved sensitivity to the anthropogenic aerosol forcing. Furthermore, we were able to underline as in Walters et al. (2014), that with the prognostic treatment of rain the problem of light rain events can be significantly reduced. Although the triclass scheme including drizzle does not significantly influence the resulting climate compared to a prognostic scheme with two classes, i.e. cloud and rain water, a prognostic scheme with three liquid classes still has its benefit depending on the requirements. Following previous research on the effect of giant CCN on warm phase clouds (Posselt and Lohmann, 2008b), giant CCN can act as a direct source for drizzle drops and would be well represented by such a scheme. Furthermore, a simple coupling of drizzle to the radiative transfer calculations by taking into account both cloud and drizzle water to determine the effective radius as suggested by Wood (2000), may have an influence on the SWCRE of marine stratocumulus. Although first tests with giant CCN did not lead to any new findings and the simple coupling of drizzle to the radiation only showed little effect (both not shown), this might change with improvements in the representation of low level clouds.

The influence of the prognostic precipitation scheme on the ice phase is largest on the amount of ice water and ICNC, such that larger crystals are present leading to more ice clouds at lower altitudes. On the other hand, larger amounts of ice water at lower altitudes produce more snow through enhanced aggregation and accretion rates. This resulted in a slightly faster hydrological cycle and is most likely the cause for the reduction in LWC above the melting level. As the conversion processes in the ice

ACPD
15, 7783–7836, 2015

phase were not changed with the introduction of prognostic snow, we do not exclude that adjustments may be necessary, especially in view of the rather small snow water mass compared to other studies (Reitter et al., 2011; Wang et al., 2011; Gettelman et al., 2015). However, the results already show that with the prognostic treatment of snow feedbacks related to both ice and liquid phase arise.

The effects of the new scheme on the radiative budget of the liquid and ice clouds at the top of the atmosphere compensate each other, such that the radiation fluxes are rather well balanced. The prognostic treatment of liquid and solid phase precipitation is certainly more physical, as models tend to go to smaller and smaller resolutions in both time and space. Moreover, the sensitivity of the liquid water path to changes in CCN concentrations is reduced, favoring a prognostic over a diagnostic treatment of precipitation when studying aerosol-cloud-precipitation interactions. Although the total net radiative effect of the anthropogenic aerosol forcing is slightly higher in PROG than in CTRL, the values are within the interannual variability and further investigations related to the tuning of the model setup might lead to an improvement in the uncertainty.

It has been shown that with the prognostic scheme the treatment of precipitation is more physical, but the feedbacks are very versatile. Especially the representation of the ice phase within the prognostic scheme needs to be addressed in future work, as dependencies on the treatment of collection processes and sedimentation cannot be excluded. Furthermore, the influence of recent improvements in the formation of cirrus clouds (Kuebbeler et al., 2014) or the sensitivity to ice properties (Eidhammer et al., 2014) to the prognostic treatment of precipitation will need to be studied. To conclude, with the introduction of prognostic precipitation future steps should imply a coupling of precipitation to the radiative transfer calculations in order to ensure consistency there.

ACPD
15, 7783–7836, 2015

Appendix: Approximated collection processes

Following the formulation by Sant et al. (2013) the collection processes are derived from the stochastic collection equation for truncated moments

$$\frac{\partial M_i^n}{\partial t} = \frac{1}{2}\left[\int_l^u \int_0^{u-y} (x+y)^n f(x) f(y) K(x,y)\,\mathrm{d}x\,\mathrm{d}y + \int_0^l \int_{l-y}^{u-y} (x+y)^n f(x) f(y) K(x,y)\,\mathrm{d}x\,\mathrm{d}y\right] - \int_0^{\infty} \int_l^u x^n f(x) f(y) K(x,y)\,\mathrm{d}x\,\mathrm{d}y, \tag{A1}$$

where x and y are the drop masses collecting each other, l and u are the lower and upper integration limits of class i ($i \in \{\mathrm{c}, \mathrm{d}, \mathrm{r}\}$), respectively, $K(x,y)$ is the collection kernel (Sant et al., 2013, Eq. 9) and f is assumed to be a four parameter modified gamma distribution

$$f_i(x) = A_i x^{\tilde{\nu}_i} \exp(-\lambda_i x^{\tilde{\mu}_i}). \tag{A2}$$

To avoid solving certain integrals numerically and save computational costs the following generalized integrals

$$I_{\mathrm{cc}}^n = \frac{k_{\mathrm{cc}}}{2} \int_0^{x_1} \int_{x_1-y}^{x_1} f_{\mathrm{c}}(x) f_{\mathrm{c}}(y) (x^2+y^2)(x+y)^n\,\mathrm{d}x\mathrm{d}y \tag{A3}$$

$$I_{\mathrm{dd}}^n = \frac{k_{\mathrm{dd}}}{2} \int_{x_1}^{x_2-x_1} \int_{x_2-y}^{x_2} f_{\mathrm{d}}(x) f_{\mathrm{d}}(y) (x+y)^{n+1}\,\mathrm{d}x\mathrm{d}y \tag{A4}$$

ACPD
15, 7783–7836, 2015

$$I_{cd}^{n} = k_{cd} \int_{x_2-x_1}^{x_2} \int_{0}^{x_2-y} f_c(x) f_d(y) (x+y)^{n+1} \, dx dy \tag{A5}$$

are approximated for the moments of number and mass density, i.e. $n \in [0,1]$, using a 4 parameter polynomial of the form

$$P_4(r) = a_1(a_0 + r)^2 + a_2(a_0 + r)^3 + a_3(a_0 + r)^4, \tag{A6}$$

where r is the radius in µm and a_m, $m \in (0,3]$, are the fitting parameters. To this end, from simulations of Sant et al. (2013) with the 1-D kinematic cloud model, the normalized integral values are rescaled and approximated by $P_4(r)$ in log-space with a non-linear least square fit using a Levenberg-Marquardt algorithm (Press et al., 1992), such that

$$P_4(r)|_{jk}^{n} = \log\left(\frac{C_{jk}^{n} I_{jk}^{n}}{N_j N_k}\right) = \log(\mathfrak{I}_{jk}^{n}) \tag{A7}$$

for $n \in [0,1]$ and $j,k \in \{\mathrm{c}, \mathrm{d}\}$. The solutions are plotted in Fig. 15 and the parameters are summarized in Tables 4 and 5. Note that $\mathfrak{I}_{dd}^{n}$ and $\mathfrak{I}_{cd}^{n}$ are piecewise approximated for $r_d < 40\,\mu\mathrm{m}$ and $r_d > 40\,\mu\mathrm{m}$, because of the functional dependency of the shape parameter $\widetilde{\nu}_d$ (cf. Sant et al., 2013, Eq. 12).

The integrals I_{cc}^{n} and I_{dd}^{n} (cf. Fig. 15a, b, d and e) collapse nicely onto a line due to the normalization by the number density and therefore, allow for a very good fit. As pointed out before, $I_{0,cd}$ and $I_{1,cd}$ still exhibit a slight dependency on the shape parameters and the continuity condition applied to the classes (cf. Sant et al., 2013), which results in the broader range of values between 40 and 60 µm in Fig. 15c and f depicted by the gray area. Although small, the approximations will not capture this variability. However, since the effect on produced surface precipitation is negligible (on the order of a few percent) they are a reliable alternative to the CPU intensive numerical solution of the integrals.

ACPD
15, 7783–7836, 2015

Acknowledgements. We would like to thank Axel Seifert for valuable comments on the manuscript, Thorsten Mauritsen, Colombe Siegenthaler-Le Drian, Francesco Isotta and Sylvaine Ferrachat for fruitful discussions and technical help. This work was finished during a BMBF funded project (FKZ: 01LK1206A) at the Max Planck Institute for Meteorology in Hamburg.

References

Ackerman, A., Kirkpatrick, M., Stevens, D., and Toon, O.: The impact of humidity above stratiform clouds on indirect aerosol climate forcing, Nature, 432, 1014–1017, 2004. 7785

Adler, R. F., Huffman, G. J., Chang, A., Ferraro, R., Xie, P. P., Janowiak, J., Rudolf, B., Schneider, U., Curtis, S., Bolvin, D., Gruber, A., Susskind, J., Arkin, P., and Nelkin, E.: The version-2 Global Precipitation Climatology Project (GPCP) monthly precipitation analysis (1979–present), J. Hydrometeorol., 4, 1147–1167, 2003. 7795, 7817, 7823

Albrecht, B. A.: Aerosols, cloud microphysics, and fractional cloudiness, Science, 245, 1227–1230, 1989. 7785

Barthazy, E. and Schefold, R.: Fall velocity of snowflakes of different riming degree and crystal types, Atmos. Res., 82, 391–398, 2006. 7793

Bellouin, N., Quaas, J., Morcrette, J.-J., and Boucher, O.: Estimates of aerosol radiative forcing from the MACC re-analysis, Atmos. Chem. Phys., 13, 2045–2062, doi:10.5194/acp-13-2045-2013, 2013. 7817

Bony, S. and Dufresne, J.: Marine boundary layer clouds at the heart of tropical cloud feedback uncertainties in climate models, Geophys. Res. Lett., 32, L20806, doi:10.1029/2005GL023851, 2005. 7785

Boucher, O., Randall, D., Artaxo, P., Bretherton, C., Feingold, G., Forster, P., Kerminen, V.-M., Kondo, Y., Liao, H., Lohmann, U., Rasch, P., Satheesh, S., Sherwood, S., Stevens, B., and Zhang, X.: Clouds and aerosols, in: Climate Change 2013: The Physical Science Basis. Contribution of Working Group I to the Fifth Assessment Report of the Intergovernmental Panel on Climate Change, edited by: Stocker, T., Qin, D., Plattner, G.-K., Tignor, M., Allen, S., Boschung, J., Nauels, A., Xia, Y., Bex, V., and Midgley, P., chap. 7, Cambridge University Press, Cambridge, United Kingdom and New York, NY, USA, 571–657, 2013. 7785, 7786, 7797, 7804

ACPD
15, 7783–7836, 2015

Cziczo, D. J., Froyd, K. D., Hoose, C., Jensen, E. J., Diao, M., Zondlo, M. A., Smith, J. B., Twohy, C. H., and Murphy, D. M.: Clarifying the dominant sources and mechanisms of cirrus cloud formation, Science, 340, 1320–1324, 2013. 7788

Dee, D. P., Uppala, S. M., Simmons, A. J., Berrisford, P., Poli, P., Kobayashi, S., Andrae, U., Balmaseda, M. A., Balsamo, G., Bauer, P., Bechtold, P., Beljaars, A. C. M., van de Berg, L., Bidlot, J., Bormann, N., Delsol, C., Dragani, R., Fuentes, M., Geer, A. J., Haimberger, L., Healy, S. B., Hersbach, H., Hólm, E. V., Isaksen, L., Kållberg, P., Köhler, M., Matricardi, M., McNally, A. P., Monge-Sanz, B. M., Morcrette, J.-J., Park, B.-K., Peubey, C., de Rosnay, P., Tavolato, C., Thépaut, J.-N., and Vitart, F.: The ERA-interim reanalysis: configuration and performance of the data assimilation system, Q. J. Roy. Meteor. Soc., 137, 553–597, 2011. 7798

Dentener, F., Kinne, S., Bond, T., Boucher, O., Cofala, J., Generoso, S., Ginoux, P., Gong, S., Hoelzemann, J. J., Ito, A., Marelli, L., Penner, J. E., Putaud, J.-P., Textor, C., Schulz, M., van der Werf, G. R., and Wilson, J.: Emissions of primary aerosol and precursor gases in the years 2000 and 1750 prescribed data-sets for AeroCom, Atmos. Chem. Phys., 6, 4321–4344, doi:10.5194/acp-6-4321-2006, 2006. 7795

Eidhammer, T., Morrison, H., Bansemer, A., Gettelman, A., and Heymsfield, A. J.: Comparison of ice cloud properties simulated by the Community Atmosphere Model (CAM5) with in-situ observations, Atmos. Chem. Phys., 14, 10103–10118, doi:10.5194/acp-14-10103-2014, 2014. 7802, 7806

Gettelman, A. and Morrison, H.: Advanced Two-Moment Bulk Microphysics for Global Models. Part I: Off-Line Tests and Comparison with Other Schemes. J. Climate, 28, 1268–1287, 2015. 7786, 7787

Gettelman, A., Morrison, H., Terai, C. R., and Wood, R.: Microphysical process rates and global aerosol–cloud interactions, Atmos. Chem. Phys., 13, 9855–9867, doi:10.5194/acp-13-9855-2013, 2013. 7801

Advanced Two-Moment Bulk Microphysics for Global Models. Part II: Global Model Solutions and Aerosol-Cloud Interactions. J. Climate, 28, 1288–1307, 2015. 7786, 7787, 7800, 7805, 7806

Greenwald, T. J., Stephens, G. L., Vonderhaar, T. H., and Jackson, D. L.: A physical retrieval of cloud liquid water over the global oceans using Special Sensor Microwave Imager (SSM/I) observations, J. Geophys. Res., 98, 18471–18488, 1993. 7817

ACPD
15, 7783–7836, 2015

Hahn, C. J., Warren, S. G., and London, J.: Climatological data for clouds over the globe from surface observations, 1982–1991: the total cloud edition, Tech. rep., ORNL/CDIAC-72 NDP-026A Oak Ridge National Laboratory, Oak Ridge Tennessee, USA, 1994. 7817, 7823

Han, Q., Rossow, W. B., Chou, J., and Welch, R. M.: Global survey of the relationships of cloud albedo and liquid water path with droplet size using ISCCP, J. Climate, 11, 1516–1528, 1998. 7817, 7823

Jiang, H., Xue, H., Teller, A., Feingold, G., and Levin, Z.: Aerosol effects on the lifetime of shallow cumulus, Geophys. Res. Lett., 33, L14806, doi:10.1029/2006GL026024, 2006. 7785

Kärcher, B. and Ström, J.: The roles of dynamical variability and aerosols in cirrus cloud formation, Atmos. Chem. Phys., 3, 823–838, doi:10.5194/acp-3-823-2003, 2003. 7788

Khairoutdinov, M. and Kogan, Y.: A new cloud physics parameterization in a large-eddy simulation model of marine stratocumulus, Mon. Weather Rev., 128, 229–243, 2000. 7788, 7791, 7794

Kuebbeler, M., Lohmann, U., Hendricks, J., and Kärcher, B.: Dust ice nuclei effects on cirrus clouds, Atmos. Chem. Phys., 14, 3027–3046, doi:10.5194/acp-14-3027-2014, 2014. 7806

Levkov, L., Rockel, B., Kapitza, H., and Raschke, E.: 3D mesoscale numerical studies of cirrus and stratus clouds by their time and space evolution, Beitr. Phys. Atmosph., 65, 35–58, 1992. 7791, 7793

Li, J.-L. F., Waliser, D. E., Chen, W.-T., Guan, B., Kubar, T., Stephens, G., Ma, H.-Y., Deng, M., Donner, L., Seman, C. and Horowitz, L.: An observationally based evaluation of cloud ice water in CMIP3 and CMIP5 GCMs and contemporary reanalyses using contemporary satellite data, J. Geophys. Res., 117, D16105, doi:10.1029/2012JD017640, 2012. 7823

Lin, H. and Leaitch, R.: Development of an in-cloud aerosol activation parameterization for climate modelling, in: WMO Workshop on Measurements of Cloud Properties for Forecasts of Weather and Climate, Mexico City, 23–27 June 1997, 328–335, 1997. 7788

Loeb, N. G., Wielicki, B. A., Doelling, D. R., Smith, G. L., Keyes, D. F., Kato, S., Manalo-Smith, N., and Wong, T.: Toward optimal closure of the Earth's top-of-atmosphere radiation budget, J. Climate, 22, 748–766, 2009. 7817

Lohmann, U. and Ferrachat, S.: Impact of parametric uncertainties on the present-day climate and on the anthropogenic aerosol effect, Atmos. Chem. Phys., 10, 11373–11383, doi:10.5194/acp-10-11373-2010, 2010. 7789

ACPD
15, 7783–7836, 2015

Lohmann, U. and Hoose, C.: Sensitivity studies of different aerosol indirect effects in mixed-phase clouds, Atmos. Chem. Phys., 9, 8917–8934, doi:10.5194/acp-9-8917-2009, 2009. 7786, 7787

Lohmann, U. and Roeckner, E.: Design and performance of a new cloud microphysics scheme developed for the ECHAM general circulation model, Clim. Dynam., 12, 557–572, 1996. 7791

Lohmann, U., Stier, P., Hoose, C., Ferrachat, S., Kloster, S., Roeckner, E., and Zhang, J.: Cloud microphysics and aerosol indirect effects in the global climate model ECHAM5-HAM, Atmos. Chem. Phys., 7, 3425–3446, doi:10.5194/acp-7-3425-2007, 2007. 7788

Lohmann, U., Spichtinger, P., Jess, S., Peter, T., and Smit, H.: Cirrus cloud formation and ice supersaturated regions in a global climate model, Environ. Res. Lett., 3, 045022, doi:10.1088/1748-9326/3/4/045022, 2008. 7788

Mauritsen, T., Stevens, B., Roeckner, E., Crueger, T., Esch, M., Giorgetta, M., Haak, H., Jungclaus, J., Klocke, D., Matei, D., Mikolajewicz, U., Notz, D., Pincus, R., Schmidt, H., and Tomassini, L.: Tuning the climate of a global model, J. Adv. Model. Earth Syst., 4, M00A01, doi:10.1029/2012MS000154, 2012. 7789

Müller, M.: Sedimentation of hydrometeors in ECHAM, Master's thesis, ETH Zurich, Zurich, 2007. 7791

Murphy, D., Solomon, S., Portmann, R., Rosenlof, K., Forster, P., and Wong, T.: An observationally based energy balance for the Earth since 1950, J. Geophys. Res., 114, D17107, doi:10.1029/2009JD012105, 2009. 7804

Posselt, R. and Lohmann, U.: Introduction of prognostic rain in ECHAM5: design and single column model simulations, Atmos. Chem. Phys., 8, 2949–2963, doi:10.5194/acp-8-2949-2008, 2008a. 7786, 7788, 7791, 7801, 7805

Posselt, R. and Lohmann, U.: Influence of Giant CCN on warm rain processes in the ECHAM5 GCM, Atmos. Chem. Phys., 8, 3769–3788, doi:10.5194/acp-8-3769-2008, 2008b. 7805

Posselt, R. and Lohmann, U.: Sensitivity of the total anthropogenic aerosol effect to the treatment of rain in a global climate model, Geophys. Res. Lett., 36, L02805, doi:10.1029/2008GL035796, 2009. 7786, 7791, 7792, 7793, 7803

Press, W., Teukolsky, S., Vetterling, W., and Flannery, B.: Numerical recipes in FORTRAN, vol. 1, Cambridge University Press, Cambridge, New York, NY, USA, 1992. 7794, 7808

Quaas, J., Ming, Y., Menon, S., Takemura, T., Wang, M., Penner, J. E., Gettelman, A., Lohmann, U., Bellouin, N., Boucher, O., Sayer, A. M., Thomas, G. E., McComiskey, A., Feingold, G., Hoose, C., Kristjánsson, J. E., Liu, X., Balkanski, Y., Donner, L. J., Ginoux, P. A.,

ACPD
15, 7783–7836, 2015

Stier, P., Grandey, B., Feichter, J., Sednev, I., Bauer, S. E., Koch, D., Grainger, R. G., Kirkevåg, A., Iversen, T., Seland, Ø., Easter, R., Ghan, S. J., Rasch, P. J., Morrison, H., Lamarque, J.-F., Iacono, M. J., Kinne, S., and Schulz, M.: Aerosol indirect effects – general circulation model intercomparison and evaluation with satellite data, Atmos. Chem. Phys., 9, 8697–8717, doi:10.5194/acp-9-8697-2009, 2009. 7786

Reitter, S., Fröhlich, K., Seifert, A., Crewell, S., and Mech, M.: Evaluation of ice and snow content in the global numerical weather prediction model GME with CloudSat, Geosci. Model Dev., 4, 579–589, doi:10.5194/gmd-4-579-2011, 2011. 7786, 7800, 7806

Roeckner, E., Bäuml, G., Bonaventura, L., Brokopf, R., Esch, M., Giorgetta, M., Hagemann, S., Kirchner, I., Kornblueh, L., Manzini, E., Rhodin, A., Schlese, U., Schulzweida, U., and Tompkins, A.: The atmospheric general circulation modell ECHAM5, Part I: Model description, Tech. Rep. 349, Max-Planck-Institute for Meteorology, Hamburg, Germany, 2003. 7787

Rogers, R., Ethier, S., Baumgardner, D., Carter, D., and Ecklund, W.: Comparison of raindrop size distributions measured by radar wind profiler and by airplane, J. Appl. Meteorol., 32, 694–699, 1993. 7792

Rosenfeld, D., Wang, H., and Rasch, P. J.: The roles of cloud drop effective radius and LWP in determining rain properties in marine stratocumulus, Geophys. Res. Lett., 39, L13801, doi:10.1029/2012GL052028, 2012. 7801

Rossow, W. B. and Schiffer, R. A.: Advances in understanding clouds from ISCCP, B. Am. Meteorol. Soc., 80, 2261–2287, 1999. 7817, 7823

Sant, V., Lohmann, U., and Seifert, A.: Performance of a triclass parameterization for the collision–coalescence process in shallow clouds, J. Atmos. Sci., 70, 1744–1767, 2013. 7787, 7788, 7790, 7794, 7805, 7807, 7808, 7836

Scott, N. A., Chédin, A., Armante, R., Francis, J., Stubenrauch, C., Chaboureau, J.-P., Chevallier, F., Claud, C., and Cheruy, F.: Characteristics of the TOVS pathfinder path-B dataset, B. Am. Meteorol. Soc., 80, 2679–2701, 1999. 7823

Seifert, A.: On the parameterization of evaporation of raindrops as simulated by a one-dimensional rainshaft model, J. Atmos. Sci., 65, 3608–3619, 2008. 7791

Spichtinger, P. and Gierens, K. M.: Modelling of cirrus clouds – Part 1a: Model description and validation, Atmos. Chem. Phys., 9, 685–706, doi:10.5194/acp-9-685-2009, 2009. 7791, 7793

Srivastava, R. C.: Parameterization of raindrop size distributions, J. Atmos. Sci., 35, 108–117, 1978. 7791

ACPD
15, 7783–7836, 2015

Stephens, G.: Cloud feedbacks in the climate system: a critical review, J. Climate, 18, 237–273, 2005. 7784
Stevens, B. and Bony, S.: What are climate models missing?, Science, 340, 1053–1054, 2013. 7784
Stevens, B. and Feingold, G.: Untangling aerosol effects on clouds and precipitation in a buffered system, Nature, 461, 607–613, 2009. 7785
Stier, P., Feichter, J., Kinne, S., Kloster, S., Vignati, E., Wilson, J., Ganzeveld, L., Tegen, I., Werner, M., Balkanski, Y., Schulz, M., Boucher, O., Minikin, A., and Petzold, A.: The aerosol-climate model ECHAM5-HAM, Atmos. Chem. Phys., 5, 1125–1156, doi:10.5194/acp-5-1125-2005, 2005. 7787
Sundqvist, H., Berge, E., and Kristjansson, J. E.: Condensation and cloud parameterization studies with a mesoscale numerical weather prediction model, Mon. Weather Rev., 117, 1641–1657, 1989. 7788, 7799
Twomey, S.: Pollution and planetary albedo, Atmos. Environ., 8, 1251–1256, 1974. 7785
van Zanten, M. C., Stevens, B., Vali, G., and Lenschow, D. H.: Observations of drizzle in nocturnal marine stratocumulus, J. Atmos. Sci., 62, 88–106, 2005. 7787
Vonder Haar, T. H., Bytheway, J. L., and Forsythe, J. M.: Weather and climate analyses using improved global water vapor observations, Geophys. Res. Lett., 39, L15802, doi:10.1029/2012GL052094, 2012. 7817
Waliser, D. E., Li, J.-L. F., Woods, C. P., Austin, R. T., Bacmeister, J., Chern, J., Del Genio, A., Jiang, J. H., Kuang, Z., Meng, H., Minnis, P., Platnick, S., Rossow, W. B., Stephens, G. L., Sun-Mack, S., Tao, W.-K., Tompkins, A. M., Vane, D. G., Walker, C., and Wu, D.: Cloud ice: a climate model challenge with signs and expectations of progress, J. Geophys. Res., 114, D00A21, doi:10.1029/2008JD010015, 2009. 7817
Walters, D. N., Williams, K. D., Boutle, I. A., Bushell, A. C., Edwards, J. M., Field, P. R., Lock, A. P., Morcrette, C. J., Stratton, R. A., Wilkinson, J. M., Willett, M. R., Bellouin, N., Bodas-Salcedo, A., Brooks, M. E., Copsey, D., Earnshaw, P. D., Hardiman, S. C., Harris, C. M., Levine, R. C., MacLachlan, C., Manners, J. C., Martin, G. M., Milton, S. F., Palmer, M. D., Roberts, M. J., Rodríguez, J. M., Tennant, W. J., and Vidale, P. L.: The Met Office Unified Model Global Atmosphere 4.0 and JULES Global Land 4.0 configurations, Geosci. Model Dev., 7, 361–386, doi:10.5194/gmd-7-361-2014, 2014. 7786, 7800, 7805
Wang, M., Ghan, S., Ovchinnikov, M., Liu, X., Easter, R., Kassianov, E., Qian, Y., and Morrison, H.: Aerosol indirect effects in a multi-scale aerosol-climate model PNNL-MMF, Atmos.

ACPD
15, 7783–7836, 2015

Chem. Phys., 11, 5431–5455, doi:10.5194/acp-11-5431-2011, 2011. 7786, 7800, 7803, 7804, 7806, 7835
Weng, F. and Grody, N.: Retrieval of cloud liquid water using the Special Sensor Microwave Imager (SSM/I), J. Geophys. Res., 99, 25535–25551, 1994. 7817
Wentz, F.: A well-calibrated ocean algorithm for SSM/I, J. Geophys. Res., 102, 8703–8718, 1997. 7817, 7823
Wielicki, B. A., Barkstrom, B. R., Harrison, E. F., Lee III, R. B., Louis Smith, G., and Cooper, J. E.: Clouds and the Earth's Radiant Energy System (CERES): an earth observing system experiment, B. Am. Meteorol. Soc., 77, 853–868, 1996. 7823
Wild, M., Folini, D., Schär, C., Loeb, N., Dutton, E. G., and König-Langlo, G.: The global energy balance from a surface perspective, Clim. Dynam., 40, 3107–3134, 2013. 7817
Wood, R.: Parametrization of the effect of drizzle upon the droplet effective radius in stratocumulus clouds, Q. J. Roy. Meteor. Soc., 126, 3309–3324, 2000. 7787, 7805
Wylie, D., Jackson, D. L., Menzel, W. P., and Bates, J. J.: Trends in global cloud cover in two decades of HIRS observations, J. Climate, 18, 3021–3031, 2005. 7817

ACPD
15, 7783–7836, 2015

Table 1. Description of the different acronyms used in Eqs. (1)–(6) to describe the sinks and sources of the different hydrometeors.

Acronym	Description
aut_c, aut_d	Autoconversion of cloud droplets and drizzle drops, respectively.
ac_{cd+}, ac_{cd-}	Source and sink of the accretion of cloud droplets by drizzle drops, respectively.
ac_{cr}, ac_{dr}	Accretion of cloud droplets and drizzle drops by rain drops, respectively.
sc_d, sc_r	Selfcollection for drizzle and rain drops, respectively.
agg, ac_s	Aggregation of ice crystals to form snow and accretion of ice crystals and cloud droplets by snow.
sec	Secondary production of ice crystals by splintering of snow flakes.
evp_d, evp_r	Evaporation for drizzle and rain drops, respectively.
sub, mlt	Sublimation and melting of snow, respectively.
sed_d, sed_r, sed_s	Sedimentation of drizzle, rain and snow, respectively.

ACPD
15, 7783–7836, 2015

Table 2. Global annual mean cloud properties and TOA energy budget for the simulations performed with ECHAM5-CTRL and -PROG as well as observations.

		PROG (PD)	PROG (PI)	CTRL (PD)	CTRL (PI)	Obs
P_{tot}	($mm\,d^{-1}$)	2.94	2.96	2.94	2.95	2.61[a]
P_{strat}	($mm\,d^{-1}$)	1.42	1.42	1.35	1.36	–
P_{conv}	($mm\,d^{-1}$)	1.52	1.54	1.59	1.60	–
TCC	(%)	63.7	63.3	64.3	64.0	65–75[b]
LWP	($g\,m^{-2}$)	69.2	62.5	74.2	67.5	50–81[c]
DWP	($g\,m^{-2}$)	2.3	2.8	–	–	–
RWP	($g\,m^{-2}$)	30.7	31.7	–	–	–
IWP	($g\,m^{-2}$)	16.2	16.1	10.6	10.5	10–65[d]
SWP	($g\,m^{-2}$)	2.0	2.0	–	–	–
WVM	($kg\,m^{-2}$)	26.3	26.3	26.3	26.4	25.4[e]
CDNC burden	($10^{10}\,m^{-2}$)	3.0	2.3	3.1	2.4	–
ICNC burden	($10^{12}\,m^{-2}$)	7.7	7.4	10.1	8.7	–
AOD	(–)	0.12	0.09	0.14	0.11	0.18[f]
SW	($W\,m^{-2}$)	235.0	236.8	231.8	233.4	240–244[g]
SWCRE	($W\,m^{-2}$)	−51.0	−49.7	−53.7	−52.6	−46 to −53[h]
LW	($W\,m^{-2}$)	−235.5	−235.7	−232.2	−232.3	−(236–242)[g]
LWCRE	($W\,m^{-2}$)	25.2	25.2	28.4	28.3	27–31[h]
F_{net}	($W\,m^{-2}$)	−0.5	1.1	−0.3	1.0	–

[a] Precipitation rate taken from the Global Precipitation Climatology Project (GPCP) for the years 1981–2010, provided by the NOAA/OAR/ESRL PSD, Boulder, Colorado, USA (Adler et al., 2003) (http://www.esrl.noaa.gov/psd/).
[b] Total cloud cover taken from ISCCP (Rossow and Schiffer, 1999), surface observations (Hahn et al., 1994), MODIS-COLL5 (http://modis-atmos.gsfc.nasa.gov/products.html), and HIRS (Wylie et al., 2005).
[c] Liquid water path taken from SSM/I (Greenwald et al., 1993; Weng and Grody, 1994; Wentz, 1997, only for oceans) and ISCCP (Han et al., 1998).
[d] Ice water path taken from Fig. 18 of Waliser et al. (2009).
[e] Precipitable water taken from the NASA Water Vapor Project-MEaSUREs (NVAP-M) dataset as given in Vonder Haar et al. (2012).
[f] AOD taken from Table 2 of Bellouin et al. (2013).
[g] SW and LW taken from Fig. 1 of Wild et al. (2013).
[h] SWCRE and LWCRE taken from Table 4 of Loeb et al. (2009).

ACPD
15, 7783–7836, 2015

Table 3. Mean global conversion rate burdens for both cloud liquid and ice for CTRL and PROG for the month of January 2000.

		PROG	CTRL
AU (= au_c)	($kg\,m^{-2}\,s^{-1}$)	5.0×10^{-6}	6.1×10^{-6}
AC (= $ac_{cd} + ac_{cr}$)	($kg\,m^{-2}\,s^{-1}$)	1.6×10^{-4}	8.0×10^{-6}
AU/(AU + AC)	%	3.0	43.5
AG (= agg)	($kg\,m^{-2}\,s^{-1}$)	2.8×10^{-4}	7.4×10^{-6}
ACi (= ac_s)	($kg\,m^{-2}\,s^{-1}$)	4.8×10^{-5}	3.5×10^{-6}
AG/(AG + ACi)	%	85.4	68.0

ACPD
15, 7783–7836, 2015

Table 4. The coefficients and scaling used in the four parameter polynomials (cf. Eq. A6) for approximating the 0th moment, i.e. $n = 0$, of the integrals in Eqs. (A3)–(A5).

Coeff.	$P_4(r)\|^0_{cc}$	$P_4(r)\|^0_{dd}$		$P_4(r)\|^0_{cd}$	
		$r_d < 40\,\mu m$	$r_d \geq 40\,\mu m$	$r_d < 40\,\mu m$	$r_d \geq 40\,\mu m$
a_0	−22.337	−50.158	−93.164	−49.556	−99.931
a_1	-1.6652×10^{-1}	-1.8943×10^{-1}	-5.3859×10^{-3}	-1.8262×10^{-1}	-5.6868×10^{-3}
a_2	-2.5767×10^{-2}	-1.6953×10^{-2}	-1.2739×10^{-4}	-1.6436×10^{-2}	-1.3552×10^{-4}
a_3	-2.2943×10^{-3}	-5.1756×10^{-4}	-1.4120×10^{-6}	-5.0922×10^{-4}	-1.1954×10^{-6}
C^0_{jk}	10^{-5}	10^{-2}		10^{-3}	

ACPD
15, 7783–7836, 2015

Table 5. The coefficients and scaling used in the four parameter polynomials (cf. Eq. A6) for approximating the 1st moment, i.e. $n = 1$, of the integrals in Eqs. (A3)–(A5).

Coeff.	$P_4(r)\|^1_{cc}$	$P_4(r)\|^1_{dd}$		$P_4(r)\|^1_{cd}$	
		$r_d < 40\,\mu m$	$r_d \geq 40\,\mu m$	$r_d < 40\,\mu m$	$r_d \geq 40\,\mu m$
a_0	−22.557	−50.376	−101.199	−50.121	−109.893
a_1	-1.7426×10^{-1}	-2.0805×10^{-1}	-4.3356×10^{-3}	-1.9190×10^{-1}	-4.8496×10^{-3}
a_2	-2.6650×10^{-2}	-1.8605×10^{-2}	-8.9089×10^{-5}	-1.6820×10^{-2}	-9.9346×10^{-5}
a_3	-2.240×10^{-3}	-5.5578×10^{-4}	-8.7550×10^{-7}	-4.9774×10^{-4}	-7.4402×10^{-7}
C^1_{jk}	10^{-12}	10^{-7}		10^{-8}	

ACPD
15, 7783–7836, 2015

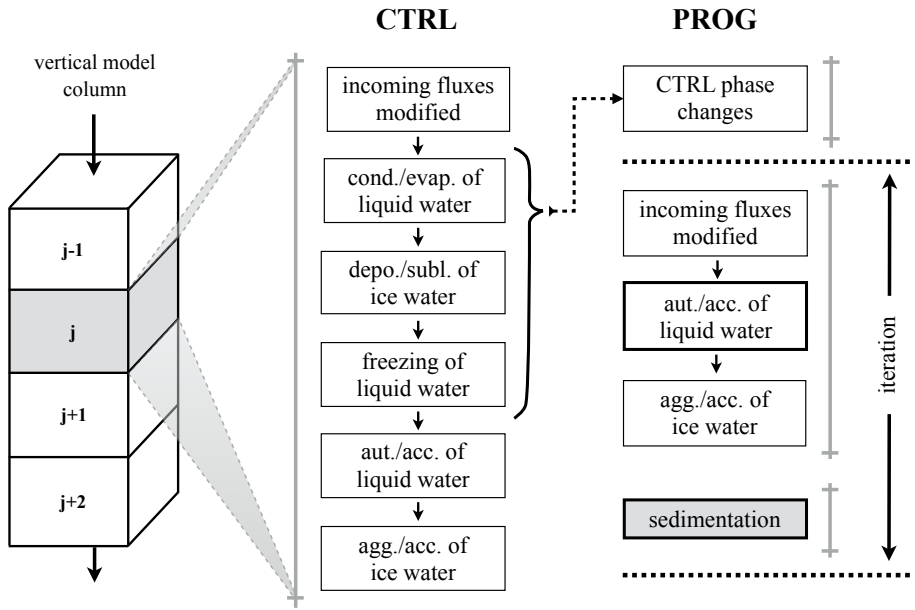

Figure 1. Schematic flowchart of the CTRL and PROG microphysics schemes. The gray vertical bars denote vertical loops (illustrated by the vertical model column on the left), the boxes in bold are new or changed schemes, and the sedimentation can be subject to a further time splitting if necessary.

ACPD
15, 7783–7836, 2015

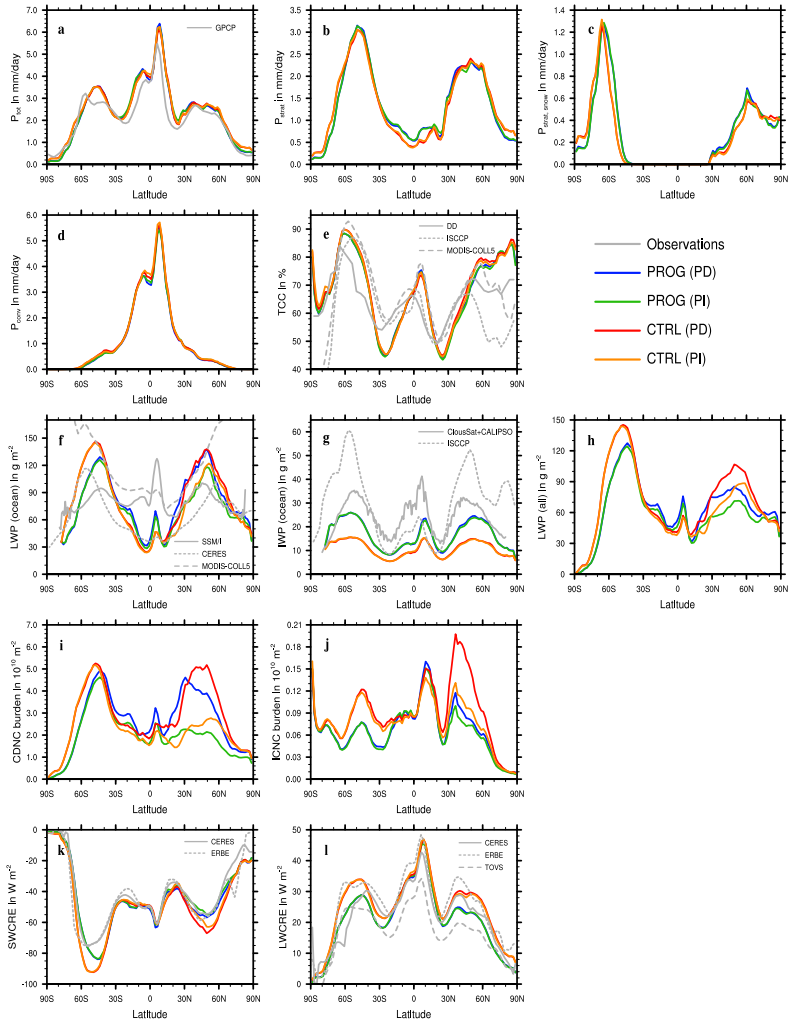

ACPD
15, 7783–7836, 2015

Prognostic precipitation in the ECHAM5-HAM

V. Sant et al.

Figure 2. Zonal annual mean average of **(a)** total precipitation (P_{tot}), **(b)** stratiform precipitation (P_{strat}), **(c)** stratiform snow precipitation ($P_{strat,\ snow}$), **(d)** convective precipitation (P_{conv}), **(e)** total cloud cover (TCC), **(f)** liquid water (LWP) and **(g)** ice water path (IWP) over the ocean, **(h)** the LWP over whole globe, **(i)** the CDNC and **(j)** ICNC burden, **(k)** shortwave (SWCRE) and **(l)** longwave cloud radiative forcing (LWCRE) for PROG and CTRL (PD and PI). The following observations are used: GPCP, the Global Precipitation Climatology Project (Adler et al., 2003) in **(a)**; DD, surface observations (Hahn et al., 1994) in **(e)**; ISCCP, International Satellite Cloud Climatology Project (Han et al., 1998; Rossow and Schiffer, 1999) in **(e, g)**; MODIS-COLL5, Moderate Resolution Imaging Spectroradiometer, Collection 5 (http://modis-atmos.gsfc.nasa.gov/products.html) in **(e, f)**; SSM/I, Special Sensor Microwave/Imager (Wentz, 1997) in **(f)**; CERES, Clouds and Earth's Radiant Energy System (Wielicki et al., 1996) in **(f)**, **(k)** and **(l)**; CloudSat + CALIPSO, ensemble mean observations of CloudSat and the Cloud-Aerosol Lidar and Infrared Pathfinder Satellite Observations satellite (Li et al., 2012) in **(g)**; ERBE, Earth Radiation Budget Experiment (http://science.larc.nasa.gov/erbe); and TOVS, TIROS Operational Vertical Sounder (Scott et al., 1999).

ACPD
15, 7783–7836, 2015

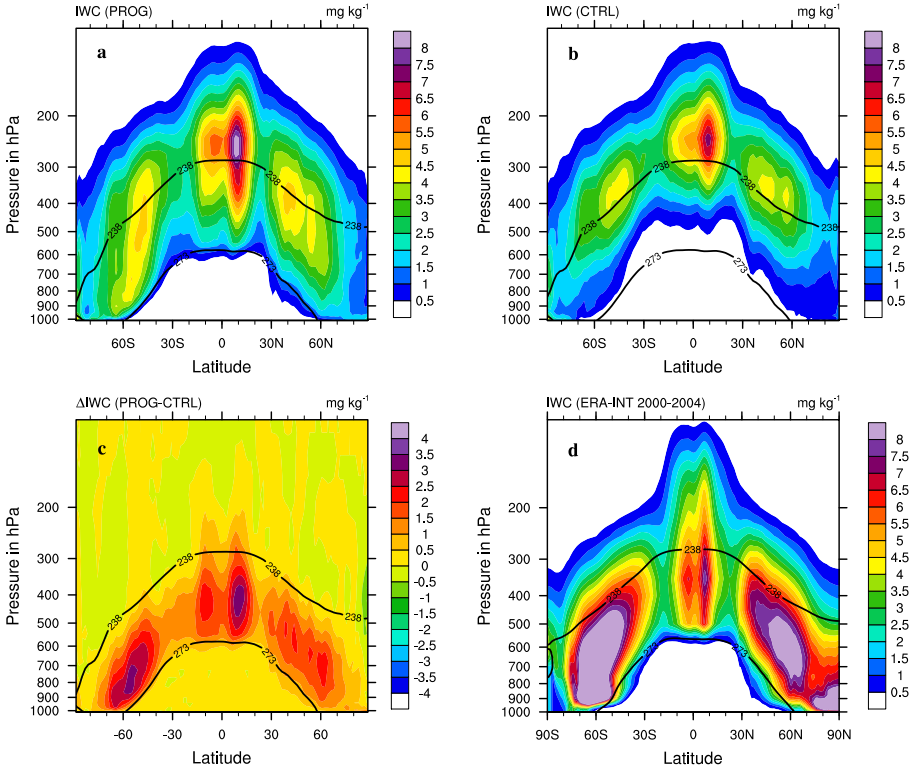

Figure 3. Ice water content of **(a)** PROG, **(b)** CTRL, **(c)** the difference PROG-CTRL and **(d)** ERA-interim reanalysis, where the solid black lines represent the melting and the homogeneous freezing levels at $T = 273$ and $T = 238$ K, respectively.

ACPD
15, 7783–7836, 2015

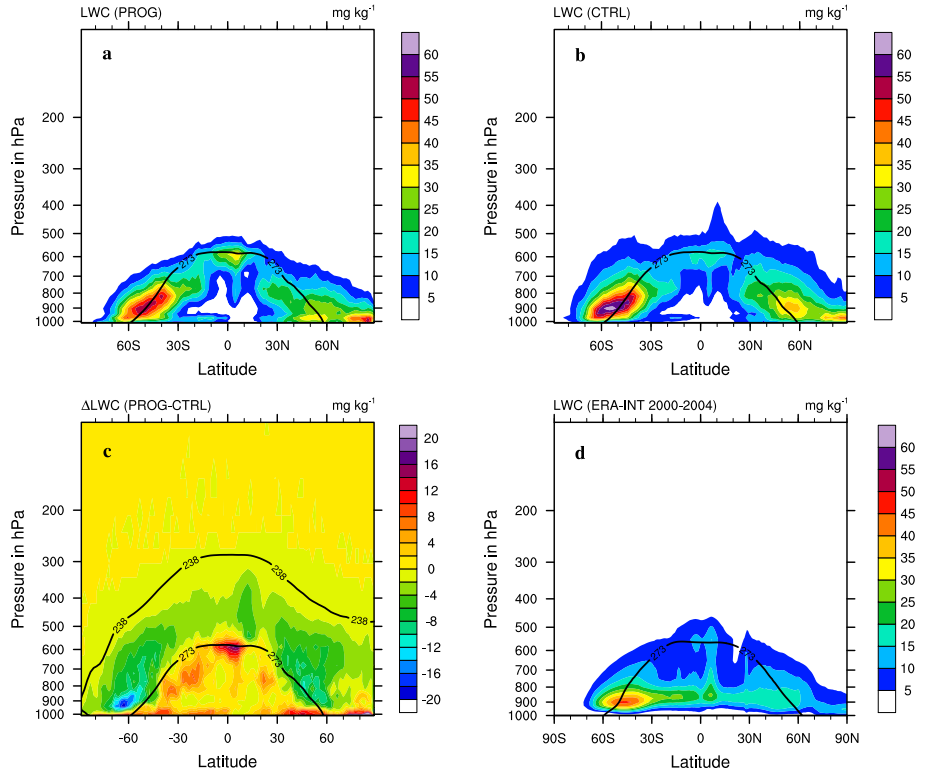

Figure 4. Liquid water content of **(a)** PROG, **(b)** CTRL, **(c)** the difference PROG-CTRL and **(d)** ERA-interim reanalysis, where the solid black lines represent the melting and the homogeneous freezing (only in **c**) levels at T = 273 and T = 238 K, respectively.

ACPD
15, 7783–7836, 2015

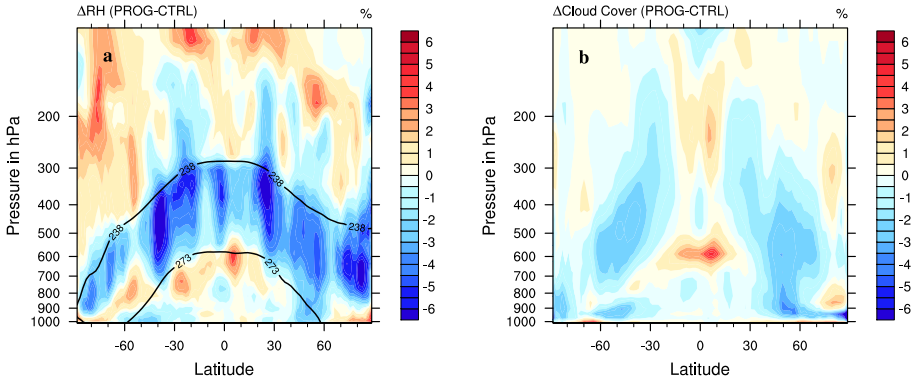

Figure 5. Difference in **(a)** RH and **(b)** TCC of PROG-CTRL, respectively. The solid black lines in **(a)** represent the melting and the homogeneous freezing levels at $T = 273$ and $T = 238$ K, respectively.

ACPD
15, 7783–7836, 2015

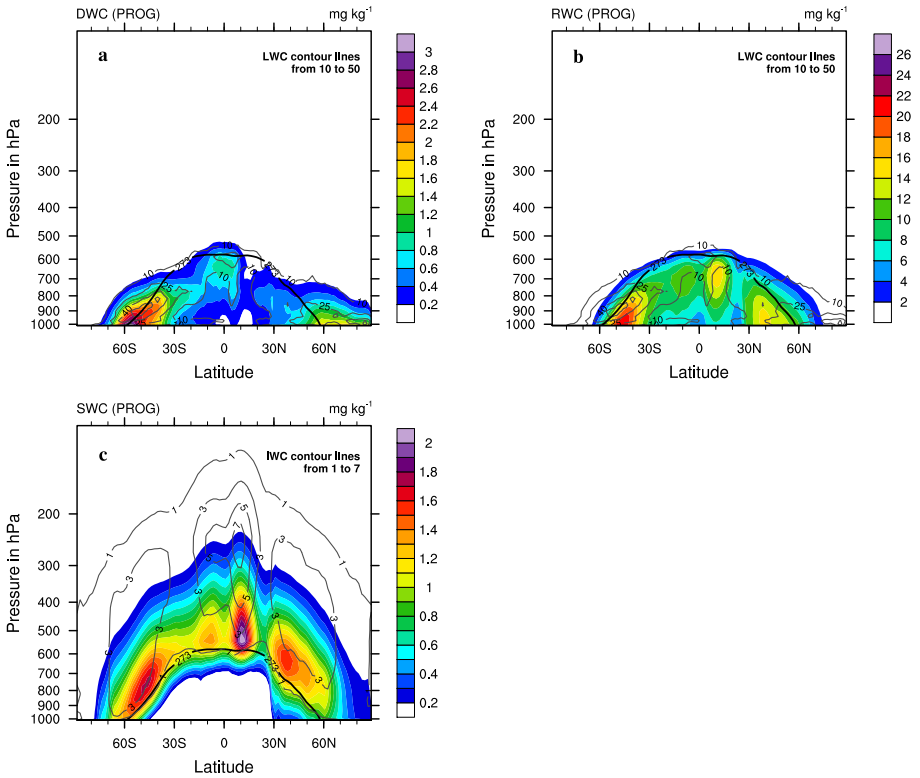

Figure 6. Precipitation water contents from PROG of **(a)** drizzle and **(b)** rain with the contour lines of the LWC, such as **(c)** snow with the contour lines of the IWC and the melting line (solid black line).

ACPD
15, 7783–7836, 2015

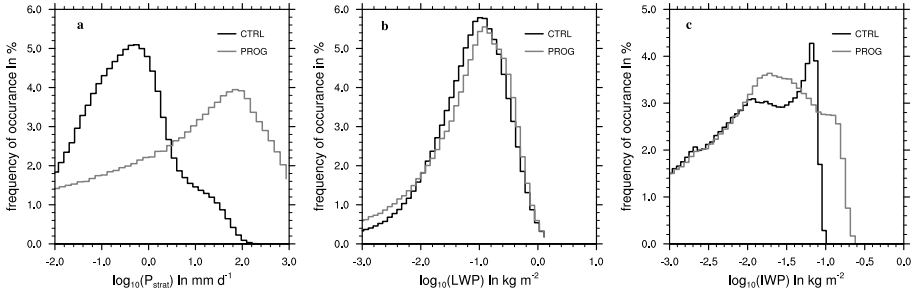

Figure 7. Frequency of occurrence of instantaneous **(a)** large-scale surface precipitation rate (only liquid phase), **(b)** liquid water path and **(c)** ice water path for the month of January 2000 for both CTRL (black line) and PROG (gray line) simulations. Note that the *x* axes are in logarithmic scale.

ACPD
15, 7783–7836, 2015

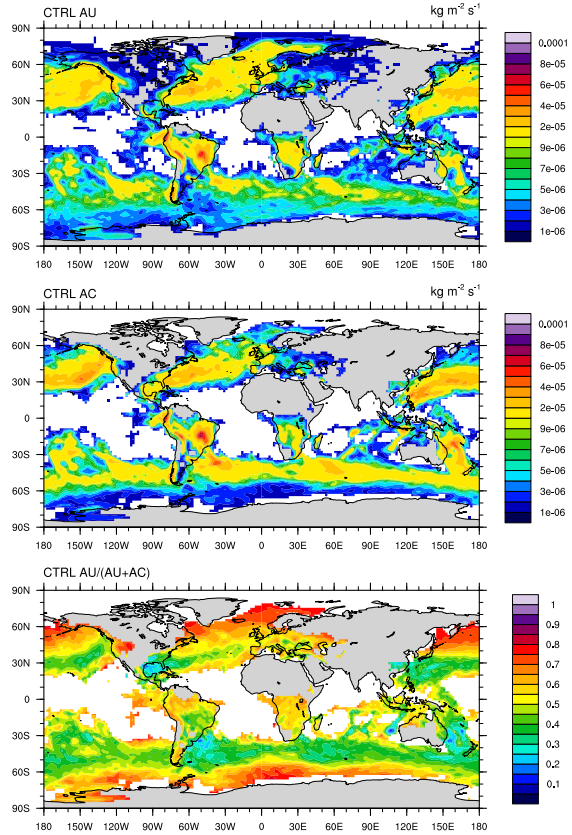

Figure 8. Mean vertically integrated autoconversion (AU) and accretion rates (AC) of CTRL for the month of January 2000, such as the fraction of AU to the total collection rate (AU + AC).

ACPD
15, 7783–7836, 2015

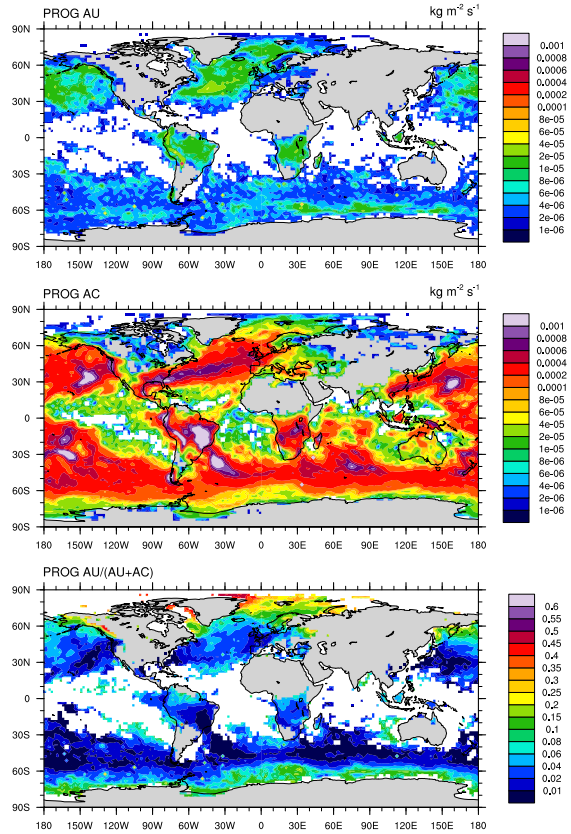

Figure 9. Mean vertically integrated autoconversion (AU) and accretion rates (AC) of PROG for the month of January 2000, such as the fraction of AU to the total collection rate (AU + AC).

ACPD
15, 7783–7836, 2015

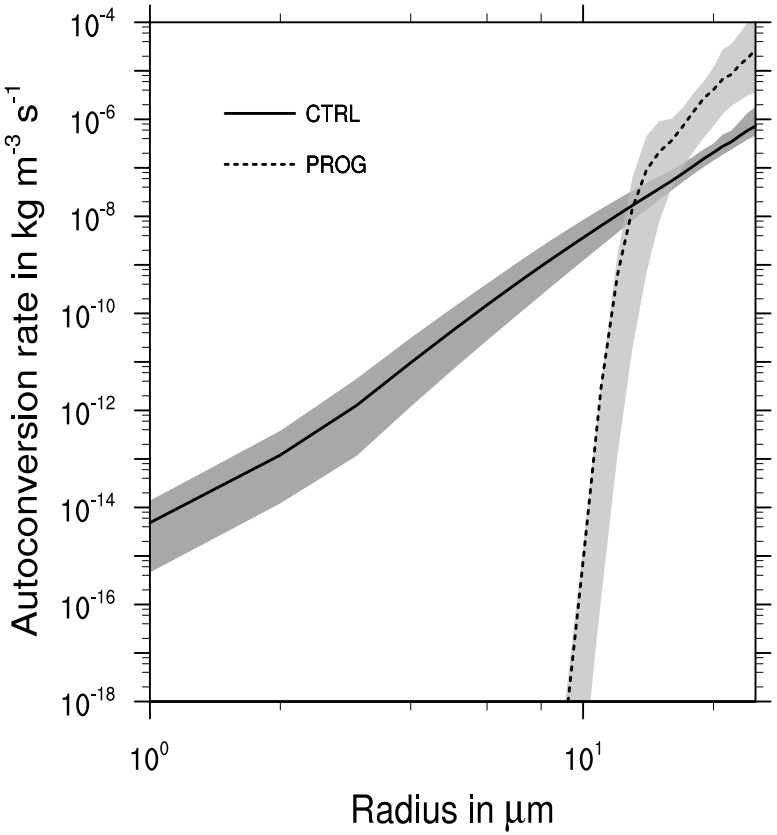

Figure 10. Dependence of autoconversion rate on effective cloud droplet radius. The lines denote the mean and the gray areas depict the range between the 5th and 95th percentile, respectively.

ACPD
15, 7783–7836, 2015

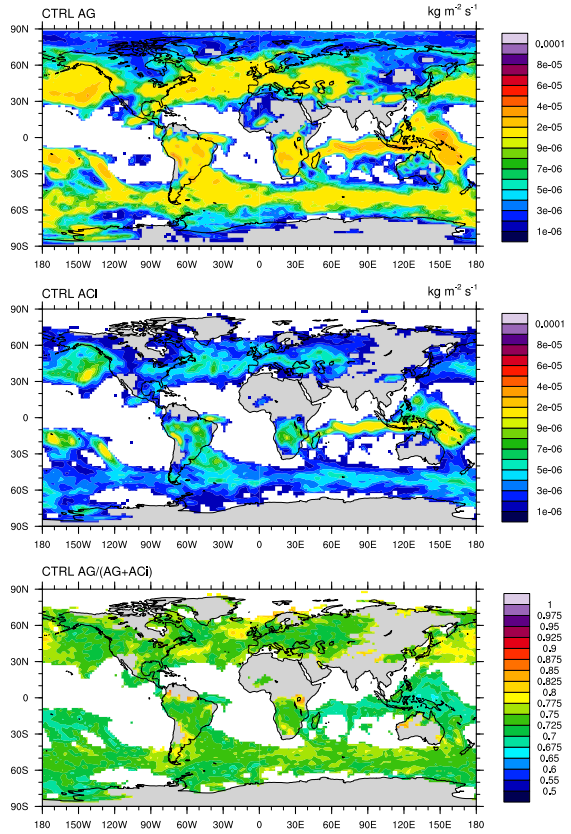

Figure 11. Mean vertically integrated aggregation (AG) and (ice) accretion rates (ACi) of CTRL for the month of January 2000, such as the fraction of AG to the total collection rate (AG + ACi).

ACPD
15, 7783–7836, 2015

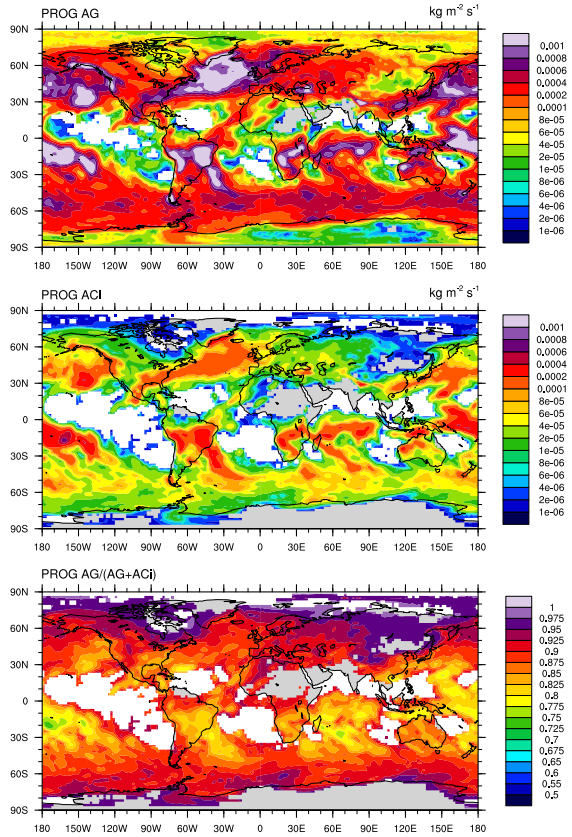

Figure 12. Mean vertically integrated aggregation (AG) and (ice) accretion rates (ACi) of PROG for the month of January 2000, such as the fraction of AG to the total collection rate (AG + ACi).

ACPD
15, 7783–7836, 2015

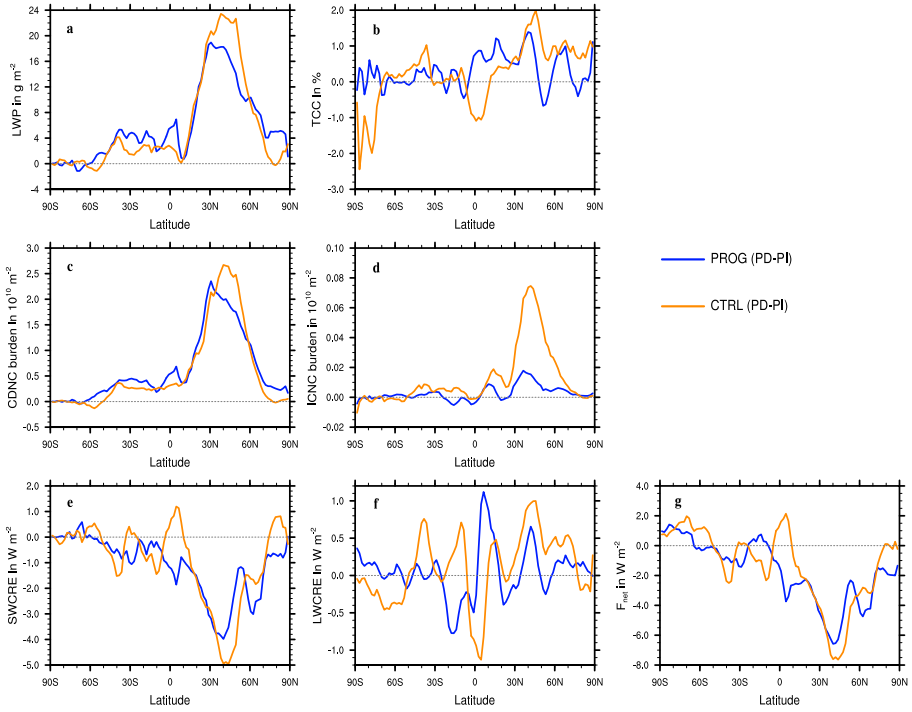

Figure 13. Zonal annual mean average difference between PD and PI of **(a)** liquid water path, **(b)** total cloud cover, **(c)** the CDNC and **(d)** ICNC burden, **(e)** shortwave, **(f)** longwave and **(g)** net TOA cloud radiative forcing for CTRL and PROG.

ACPD
15, 7783–7836, 2015

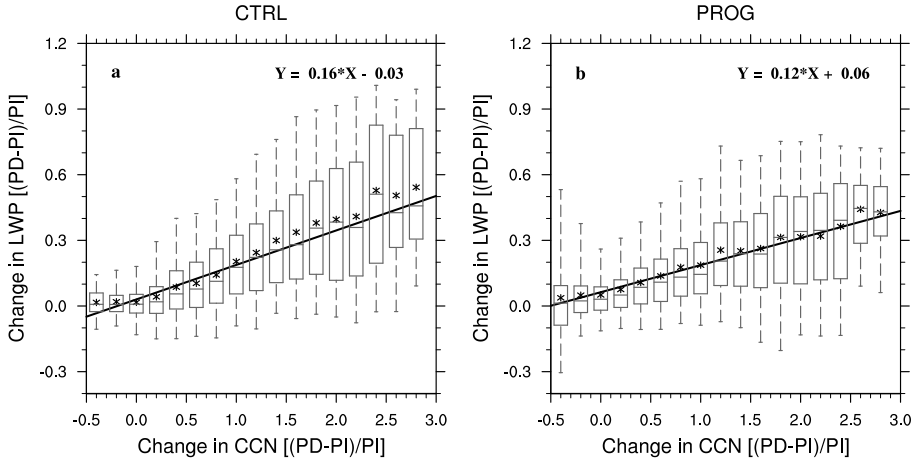

Figure 14. Boxplots and linear regression lines of the relative changes [(PD – PI)/PI] in annual mean LWP vs. the relative changes in annual mean activated CCN concentrations for **(a)** the CTRL and **(b)** the PROG simulations, following the analysis by Wang et al. (2011). CCN concentrations are averaged over the lowest 8 model levels (surface to about 800 hPa). The boxes represent the median (middle line) and the 25th and 75th percentile (lower and upper line), respectively, of the data within that bin. The whiskers show the 5th and 95th percentile (lower and upper whisker), respectively, and the stars represent the mean.

ACPD
15, 7783–7836, 2015

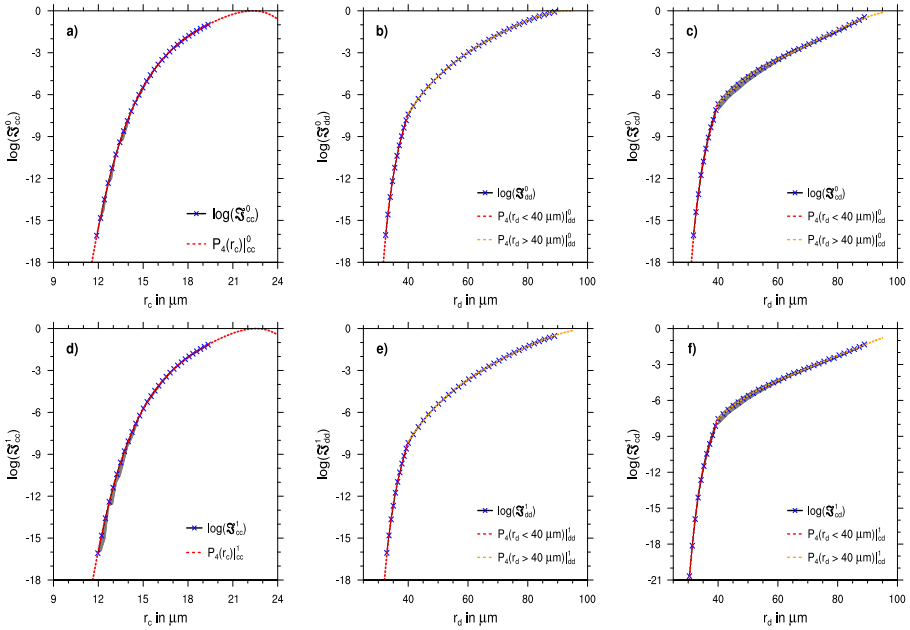

Figure 15. Approximation of Eqs. (A3)–(A5) using a four parameter polynomial $P_4(r)$ (cf. Eq. A7) from an ensemble of simulations with the 1-D kinematic cloud model (Sant et al., 2013). The gray area in the figures represents the range of the minimum and maximum values. Note that the gray area in **(a, b)** and **(e)** are very small and hardly recognizable.

ACPD
15, 7783–7836, 2015